Quasiparticle spectra of $2H$-$NbSe_2$: Two-band superconductivity and the role of tunneling selectivity

Y. Noat,[1,2] J. A. Silva-Guillén,[3] T. Cren,[1,2] V. Cherkez,[1,2] C. Brun,[1,2] S. Pons,[1,2] F. Debontridder,[1,2] D. Roditchev,[1,2] W. Sacks,[1,4] L. Cario,[5] P. Ordejón,[3] A. García,[6] and E. Canadell[6]

[1]*Sorbonne Universités, UPMC Univ Paris 06, UMR 7588, Institut des Nanosciences de Paris, 75005 Paris, France*

[2]*CNRS, UMR 7588, Institut des Nanosciences de Paris, 75005 Paris, France*

[3]*Catalan Institute of Nanoscience and Nanotechnology (ICN2), CSIC and The Barcelona Institute of Science and Technology, Campus UAB, Bellaterra, 08193 Barcelona, Spain*

[4]*IMPMC, Université Paris 6, CNRS, 4 Pl. Jussieu, 75015 Paris, France*

[5]*Institut des Matériaux Jean Rouxel, UMR 6502, 2 rue de la Houssinière, 44322 Nantes, France*

[6]*Institut de Ciència de Materials de Barcelona (ICMAB-CSIC), Campus UAB, 08193 Bellaterra, Spain*

(Received 15 December 2014; revised manuscript received 23 March 2015; published 13 October 2015)

We have studied the superconducting state of $2H$-$NbSe_2$ by scanning tunneling spectroscopy along two different crystal orientations, the c and the a/b axes. Along the c axis a large gap is dominant in the spectra, while a smaller gap is measured along the a/b axis. We show that these spectra are accurately described by the McMillan model where the small gap is induced through the coupling to the band associated with the large gap. In order to assign the small and large gaps to specific parts of the $2H$-$NbSe_2$ Fermi surface, the electronic structure was studied using first-principles calculations. While we cannot exclude the possibility of intrinsic anisotropy of the gaps, we propose that the large gap opens in the Fermi surface cylinders located around the corner K points while the sheets located around Γ are associated with the small gap. An additional component of the Fermi surface, a selenium based pocket, plays an essential role in the tunneling process. The role of the charge density wave occurring in this material is also discussed. Finally, we are able to give a coherent description of the observed characteristics of the tunneling spectra of $2H$-$NbSe_2$ as well as the differences with $2H$-NbS_2 where no charge density wave state is present. Further experimental work, such as high-resolution ARPES, would be very useful to confirm our interpretation. The approach and modeling developed here could also be relevant for other compounds of the dichalcogenide family.

DOI: 10.1103/PhysRevB.92.134510 PACS number(s): 74.20.Mn, 74.20.Pq, 74.70.Ad

I. INTRODUCTION

Superconductivity in niobium diselenide ($2H$-$NbSe_2$), $T_c \sim 7$ K, was discovered about fifty years ago [1,2]. In spite of numerous experimental and theoretical studies of the material, the precise nature of its superconducting (SC) state remains controversial. In particular, the relation between the SC transition [1,2] and the charge density wave order [3] is still debated.

The possibility of some anisotropy in the SC gap was already noted in the 1970's by Morris *et al.* [4]. Clear deviations from the standard BCS density of states (DOS) were then observed by Hess *et al.* [5] using scanning tunneling spectroscopy (STS) on a c-axis oriented sample, but were not given much attention at the time. This is surprising since the two-branch Fermi surface (FS), with a set of Nb-derived cylinders around the central Γ point of the hexagonal Brillouin zone and another set of cylinders around the corner K points, had been well established [6–8]. A few years after, the gap anisotropy was modeled by Rodrigo *et al.* [9] using a continuous gap distribution.

More recently, a two-gap scenario was proposed by several groups based on photoemission (ARPES) [10], heat conductivity [11], specific heat [12,13], and penetration length measurements [14]. In all these works, the system is described by the early model of Suhl, Matthias, and Walker [15], which assumes a pair coupling between the two bands, giving rise to a BCS-like density of states [16]. A particular feature of the Fermi surface of $2H$-$NbSe_2$ is the existence of a selenium-based pocket near the Brillouin zone center. This was first revealed by a combined de Haas-van Alphen and density functional theory (DFT) study [17] and later confirmed by ARPES Fermi surface mappings [10,18]. Its role in the multigap scenario has not been determined yet.

The room-temperature crystal structure of $2H$-$NbSe_2$ [19,20] (see Fig. 1) is built from hexagonal $NbSe_2$ layers containing Nb atoms in a trigonal prismatic coordination. The six Nb-Se bonds within these layers are identical (2.598 Å). As shown in Fig. 1, the repeat unit of the solid contains two symmetry equivalent layers related by a screw axis along c. Successive layers are separated by van der Waals coupling through which there are relatively short Se–Se contacts, i.e., every Se atom makes three Se–Se contacts (3.537 Å) shorter than the sum of the van der Waals radii with the Se atoms of the adjacent layer. The Se–Se contacts along the c direction within the hexagonal layers are even shorter, 3.347 Å. These two structural features give a considerable three-dimensional character to this layered material.

At 30 K, $2H$-$NbSe_2$ undergoes a distortion leading to a $(3a \times 3a)$ superstructure [3]. Its origin has been attributed to a Fermi surface nesting driven charge density wave (CDW) [21] although this explanation has been challenged [7,8,18,22–24]. Recently, it has been shown both experimentally and theoretically that a strong electron-phonon coupling is occurring in this material [25,26]. Although several models of the distorted phase have been discussed [27,28], only recently in the course of our work the detailed structure of this phase has been reported [30].

In this paper, the question of multigap superconductivity in $2H$-$NbSe_2$ (from now on we will refer to $2H$-$NbSe_2$

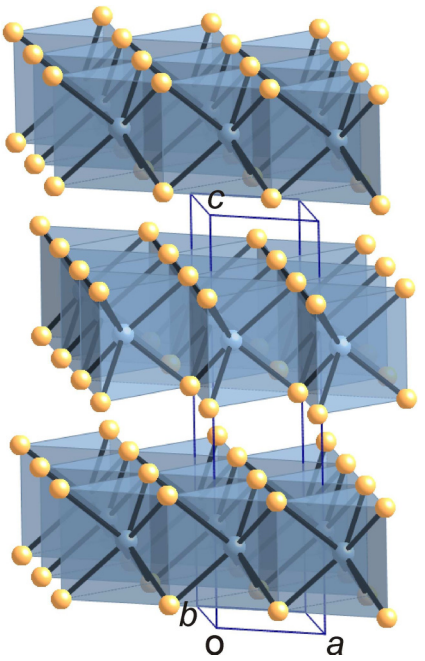

FIG. 1. (Color online) Crystal structure of $2H$-$NbSe_2$. The Nb and Se atoms are represented with blue and yellow spheres, respectively.

simply as $NbSe_2$) is studied using tunneling measurements along different crystal orientations. Also, its connection to the band structure and Fermi surface is examined. We show that tunneling measurements along c-axis oriented samples using a normal tip can be described in the framework of a two-band model. In addition, a smaller gap is observed along the a/b axis. Superconducting-vacuum-superconducting (SIS) configurations were also realized. The SIS data obtained with a nominal c-axis oriented sample and a $NbSe_2$ tip with a/b orientation confirm this scenario. We further explain why the large gap is dominantly observed along the c axis and show that such an effect results from the tunneling selectivity and can be qualitatively understood on the basis of the DFT band structure of the material together with the CDW state coexisting at low temperature.

We finally conclude that $NbSe_2$ is a two-gap superconductor in many ways similar to MgB_2: while superconductivity develops in one band (the one giving rise to a large gap), it is induced in the other band (with a small gap) by means of a proximity effect in reciprocal space (see [31] for MgB_2). This effect is adequately described by the McMillan equations [32], where interband coupling arises because of quasiparticle scattering from one band to the other [33], not taken into account in the Suhl-Matthias-Walker model [15]. The role of the selenium Fermi surface pocket is also discussed.

II. ONE OR TWO GAPS? SURVEY OF AVAILABLE EXPERIMENTAL RESULTS

A. Gap anisotropy versus two-gap superconductivity

Clear deviations from conventional BCS behavior were observed in the tunneling spectra [5] and in the field dependence of the γ coefficient in the specific heat [11,13,34,35]. The origin of these deviations was addressed by means of many experimental techniques: specific heat [12,13], heat transport [11], penetration length [14], and scanning tunneling spectroscopy [9,36]. The results are summarized in Table I. They can be sorted into two groups, either concluding that $NbSe_2$ is a two-gap superconductor [11,12,36], including a possible gap distribution [9], or that the gap is anisotropic in k space [37]. Some works [13,14] suggest that the experimental results could be interpreted in both ways.

It is important to note that in order to fit the specific heat or penetration depth data [12–14], it was implicitly assumed that the DOS is a weighted sum of BCS DOS with two different gap values. This assumption is equivalent to the pioneering model of Suhl, Matthias, and Walker [15] for a two-gap superconductor, where the two corresponding bands are coupled by an interband pair coupling term. While penetration depth and specific heat measurements do not allow to conclude which model describes best the SC properties in

TABLE I. Survey of the experimental results for $NbSe_2$ addressing the issue of gap anisotropy vs two-gap superconductivity.

Work	Experiment	Model	Gap value(s) (meV)
Huang *et al.* [12]	Specific heat	Two isotropic gaps (fit)	$\Delta_S = 0.73$, $\Delta_L = 1.26$ Weights: 20%; 80%
Ying *et al.* [13]	Specific heat	Two isotropic gaps (fit)	$\Delta_S = 0.85$, $\Delta_L = 1.5$ Weights: 36%; 64%
Ying *et al.* [13]	Specific heat	Anisotropic gap (fit) $\Delta = \Delta_0[0.4 + 0.6\lvert\cos(3\theta)\rvert]$	$\Delta_0 = 1.62$
Rodrigo *et al.* [9]	STS	Gap distribution (fit) $N(E) = \frac{1}{\alpha_i}\sum \alpha_i N_{\mathrm{BCS}}(\Delta_i, E)$	Gap values in the range [0.4–1.4]
Fletcher *et al.* [14]	Penetration length	Two isotropic gaps (fit)	$\Delta_S = 0.62$–0.67, $\Delta_L = 0.98$–1.27 Weights: 43%–50%; 50%–57%
Fletcher *et al.* [14]	Penetration length	Sixfold gap $\Delta(\phi,T) = \Delta_{\min}(T)\frac{[1+\epsilon\cos(6\phi)]}{1-\epsilon}$	$\Delta_{\min} = 0.56$–0.58 $\frac{1+\epsilon}{1-\epsilon} = 1.74$–$2.33$
Boaknin *et al.* [11]	Heat conductivity	Two gaps (Deduced from two length scales)	$\frac{\Delta_L}{\Delta_S} \sim 3$
Sanchez *et al.* [37]	Specific heat	Anisotropic gap (fit) $\Delta_k(T) = \Delta_0(T)(1 - \epsilon_2\cos^2\theta)$	$\Delta_0(0) = 1.55$; $\epsilon_2 = 0.6$

TABLE II. Comparison of gap values (in meV) deduced from photoemission experiments for $NbSe_2$ in the Se pocket around Γ as well as in the Nb cylinders around Γ and K.

Work	Gap (meV) Se pocket	Nb (Γ)	Nb (K)
Kiss *et al.* [38]	–	0.65 ± 0.05	–
Yokoya *et al.* [10]	0	1 ± 0.1	0.9 ± 0.1
Kiss *et al.* [40]	0	0.9–1.1	0.3–1.1
Borisenko *et al.* [41]	–	0–0.5	0.8
Rahn *et al.* [42]	0 ± 0.2	0.1 ± 0.3	$2.3\text{-}2.6 \pm 0.2$

$NbSe_2$, we show in Sec. III that a different mechanism for the band coupling has to be considered to precisely reproduce the shape of the tunneling spectra. The model developed in this work should also describe properly specific heat and penetration depth measurements.

B. Photoemission results

ARPES results measured for $NbSe_2$ are often contradictory [10,38–42]. The resolution of the photoemission, at best of the order of twice the superconducting gap, and the low critical temperature of this material makes the data difficult to analyze. Moreover, the transition to the CDW state, whose origin and consequences on the spectral weight and superconducting state are still debated, complicates the determination of the spectral modification at the Fermi energy E_F near the SC critical temperature. Yet, some general features emerge from the analysis of the more recent fine ARPES experiments (see Table II for a comparison of reported photoemission results): a large gap is shown to open in the Nb cylinders around K, while a smaller gap is found associated with the Nb Γ cylinders. There is no indication of the existence of a gap in the small Se pocket around Γ. However, these results should be taken with care since the ARPES data for the Se p_z pocket are affected by the very strong k_z dispersion (see the band diagram calculations in Sec. IV A) and possibly also by surface defects. The selenium p_z states appear strongly blurred in photoemission images and a quantitative analysis of this band is questionable. Indeed, the finding of nongapped states at the Fermi energy in the Se pocket contradicts the existence of a superconducting state and is most probably due to a lack of sufficient energy resolution. In contrast, STS experiments, as well as specific heat measurements, clearly imply a fully gapped DOS at E_F.

III. SCANNING TUNNELING SPECTROSCOPY EXPERIMENT

A. Tunneling along the *c* axis

High purity $NbSe_2$ was prepared in a sealed tube using the standard iodine vapor transport method. The samples were cleaved in UHV and the tunneling conductance was measured using our home-built STM/STS setups at low temperature (most of the experiments were done at $T = 2.3$ K; additional measurements in order to explore the fine structure of the superconducting gap were done at $T = 300$ mK using another setup). Figure 2 shows a typical tunneling conductance

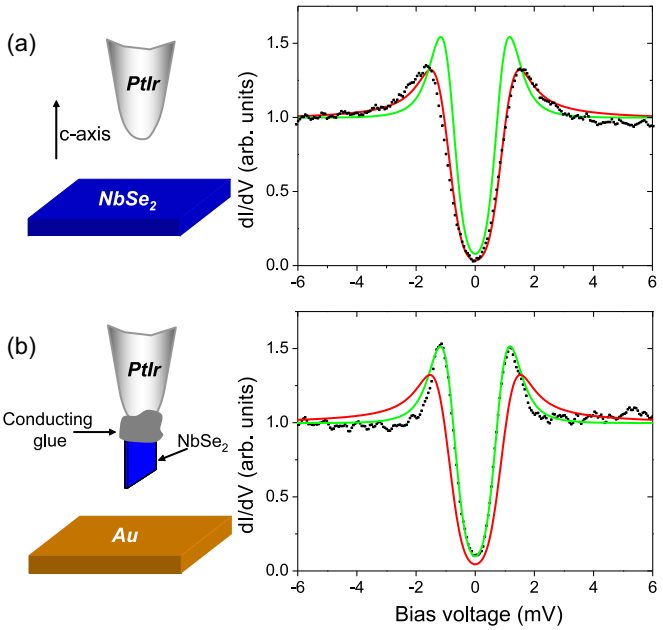

FIG. 2. (Color online) (a) Tunneling conductance obtained with a metallic (platinum-iridium) tip in a c-axis oriented $NbSe_2$ sample. The data (black dots) are fitted by a two-gap model (McMillan equations) assuming a full tunneling selectivity towards the large-gap band ($T_L = 1$, in red). It is compared to the situation where the tunneling arises towards the band with a small gap ($T_S = 1$, in green). (b) Tunneling conductance obtained with a $NbSe_2$ tip oriented along the a/b axis. The tip is obtained by gluing a $NbSe_2$ sample on the side to a platinum-iridium tip. The data are fitted by a two-gap model (McMillan equations) assuming a tunneling selectivity towards the small gap band ($T_S = 1$, in green). It is compared (red curve) to the situation where the tunneling arises towards the band with a large gap ($T_L = 1$). The parameters used for the fit in both cases are the following: $T_{\text{fit}} = 2.2$ K, $\Delta_L^0 = 1.4$ meV, $\Delta_S^0 = 0$ meV, $\Gamma_{SL} = 3$ meV, and $\frac{\Gamma_{LS}}{\Gamma_{SL}} = 1/3$.

spectrum measured at low temperature with a PtIr tip. As reported previously [5,9], a well-pronounced gap is observed. However, as shown in the following, this does not mean that only a single gap parameter is present. In this case, the tunneling conductance shape deviates from a conventional single-gap BCS superconductor.

As shown in a previous report [36], the tunneling conductance can be fitted by the McMillan equations [32]. This model was originally developed in order to describe a thin normal layer coupled to a superconducting layer. It is also relevant to describe a proximity effect in reciprocal space for a multiband superconductor such as MgB_2, where a 2D band with high electron-phonon coupling is coupled to a band with 3D character and low electron-phonon coupling [43]. In MgB_2, two gaps are clearly observed in point contact spectroscopy [44] or in tunneling experiments [45–47]. Furthermore, the shape of the excitation spectra follows the McMillan equations and is in agreement with this two band scenario [31,48].

In the McMillan model, a multiband superconductor is described by intrinsic gaps Δ_i^0 resulting from electron-phonon coupling in each band i and by the quasiparticle coupling between bands i and j, characterized by a coupling parameter

Γ_{ij}, which represents the inverse lifetime of a quasiparticle in band i due to its coupling to band j. Such a coupling could result from the presence of impurities [33]. In the clean limit, one cannot exclude the additional effect of electron-electron scattering. This point remains to be studied by ab-initio calculations including small electron correlations.

The interband coupling leads to energy-dependent gaps $\Delta_i(E)$, which can be calculated by the self-consistent equations [32]

$$\Delta_i(E) = \frac{\Delta_i^0 + \Gamma_{ij}\Delta_j(E)/\sqrt{\Delta_j^2(E) - E^2}}{1 + \Gamma_{ij}/\sqrt{\Delta_j^2(E) - E^2}} \quad (1)$$

with $i = 1,2$. The density of states $N_S(E) = \sum_i N_S^i(E)$ is expressed as a sum over the partial density of states $N_S^i(E)$ in each band i :

$$N_S^i(E) = N_i(E_F)\mathrm{Re}\left[\frac{|E|}{\sqrt{E^2 - \Delta_i(E)^2}}\right]. \quad (2)$$

To describe the scanning tunneling experiment, we take into account an additional tunneling selectivity. Depending on the configuration in k space and symmetries of the bands relevant to the surface plane probed by STS, one particular band or the other can be probed. This effect was clearly demonstrated in magnesium diboride. Indeed, it has been shown that for c-axis oriented samples of MgB_2, only the small gap is observed in the tunneling density of states [46,47], while two gaps are clearly seen for an a/b-axis oriented sample in grains with arbitrary orientations [45]. This is due to the particular symmetries of the bands in MgB_2: the large-gap develops in the σ band, with high electron phonon coupling and having a rather 2D nature, while a small gap is induced in the π band having 3D character [43,49]. This explains why the small gap is preferentially observed in a nominal c-axis oriented sample by scanning tunneling spectroscopy.

Taking into account selectivity effects, the tunneling DOS probed by STS for a two-gap superconductor can be written in the general way

$$N_S(E) = \sum_{i=1,2} T_i N_i(E_F)\mathrm{Re}\left[\frac{|E|}{\sqrt{E^2 - \Delta_i(E)^2}}\right]$$
$$= \sum_{i=1,2} N_i^{\mathrm{eff}}\mathrm{Re}\left[\frac{|E|}{\sqrt{E^2 - \Delta_i(E)^2}}\right], \quad (3)$$

where T_i accounts for the k-averaged tunneling probability towards a given band i and $N_i^{\mathrm{eff}} = T_i N_i(E_F)$ is the effective DOS in band i as measured by STS taking into account the tunneling selectivity.

It is important to note that the interband quasiparticle coupling leads to characteristic signatures in the excitation spectra which deviate from the standard BCS form [36]. This is at odds with the case of interband pair coupling as considered by Suhl *et al.* [15] which gives rise to a standard BCS DOS for each band. Thus, from the tunneling conductance fit, we can deduce the values of the intrinsic gaps in each band Δ_0^i, as well as the interband coupling parameters Γ_{ij}. Note that the ratio of the partial DOS of the two bands is directly related to

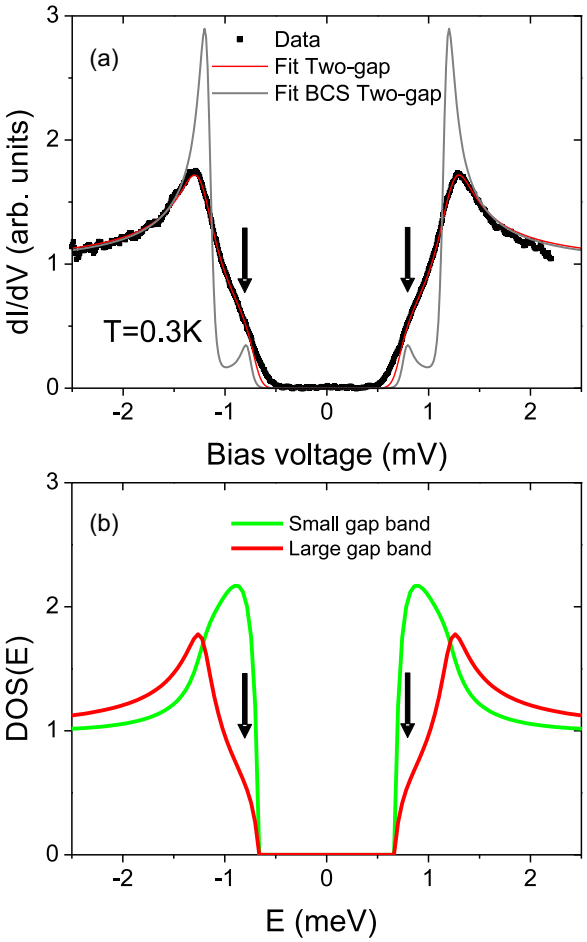

FIG. 3. (Color online) (a) Tunneling conductance obtained with a metallic (platinum-iridium) tip in a c-axis oriented $NbSe_2$ sample at $T = 300$ mK. The data are fitted by a two-gap model (McMillan equations) assuming a full tunneling selectivity towards the large gap ($T_L = 1$, in red). The parameters used for the fit are the following: $T_{\mathrm{fit}} = 0.4$ K, $\Delta_L^0 = 1.32$ meV, $\Delta_S^0 = 0$ meV, $\Gamma_{SL} = 2.5$ meV, and $\frac{\Gamma_{LS}}{\Gamma_{SL}} = 1/4$. A two-gap BCS fit (Sulh's model) is also shown (in grey) with parameters: $\Delta_S = 0.77$ meV, $\Delta_L = 1.15$ meV, and $T_L = 0.9$. (b) Partial DOS for the small (in green) and large gap (in red) obtained with the parameters deduced from the fits (shown in Fig. 2). $\Delta_L^0 = 1.3$ meV, $\Delta_S^0 = 0$ meV, $\Gamma_{SL} = 2.5$ meV, and $\frac{\Gamma_{LS}}{\Gamma_{SL}} = 1/4$.

the interband coupling between them:

$$\frac{\Gamma_{ij}}{\Gamma_{ji}} = \frac{N(E_F^j)}{N(E_F^i)}.$$

This property is very useful and will allow us to compare this ratio with the result of bulk measurements such as specific heat.

For $NbSe_2$, we get from the fits [see Fig. 2(a)]: $\Delta_L^0 = 1.4 \pm 0.1$ meV and $\Delta_S^0 = 0.00 \pm 0.1$ meV. In order to confirm the fine structure of the gap, additional measurements were also done at $T = 300$ mK. The tunneling conductance and the corresponding fit with the two-gap model is plotted in Fig. 3(a) [50]. The shape is very well reproduced by the two-gap McMillan model, while the fit with the two-gap BCS model clearly deviates from the experimental curve.

In Fig. 3(b), we show the partial DOS of $NbSe_2$ deduced from these fits. Each curve is clearly different from the usual BCS DOS. In particular, a distinctive kink is noticeable at the "small-gap" energy [see arrows in Fig. 3(b)] in the partial DOS corresponding to the "large-gap" band.

With this analysis we find that superconductivity preferentially develops in one band while Cooper pairs arise in the other band by the proximity effect, since $\Delta_S^0 = 0$. This is analogous to the case of MgB_2 where superconductivity develops in the σ band and is induced in the π band [43]. The values found in $NbSe_2$ for the interband coupling parameters are $\Gamma_{SL} = 3 \pm 0.3$ and $\frac{\Gamma_{LS}}{\Gamma_{SL}} = 1/3 \pm 0.03$. The ratio of the coupling parameters is given by the ratio of the partial DOS at the Fermi energy of the corresponding bands: $\frac{\Gamma_{12}}{\Gamma_{21}} = \frac{N_2(E_F)}{N_1(E_F)}$. Thus, knowing the contribution of the different bands in the DOS would help identify in which band superconductivity develops preferentially (i.e., the band with a large SC gap).

The relative weights in the DOS found for the small and large-gap bands are in qualitative agreement with the values deduced from the temperature and magnetic field dependence of the specific heat measurements [12]. Indeed, fitting these data with a simple two-band model (i.e., the model of Suhl *et al.* [15]), Huang *et al.* [12] found a ratio close to 1/4 with gap values $\Delta_S = 0.73$ meV and $\Delta_L = 1.26$ meV, while Ying *et al.* [13] found a ratio 0.56 with gap values $\Delta_S = 0.85$ meV and $\Delta_L = 1.5$ meV.

The tunneling selectivity that appears in the STS experiment on $NbSe_2$ is very sensitive to the cleavage conditions. When the cleavage was done under UHV conditions, the large-gap DOS dominates in the tunneling current, i.e., $T_L \approx 1$. On the other hand, when the sample is cleaved in air, the tunneling selectivity varies and a combination of the small and large-gap DOS is necessary to fit the data properly ($0 \leqslant T_S \leqslant 0.5$). We propose that this effect is related to some modifications in the Se pocket arising with surface contamination when the sample is cleaved in air.

We also note that the tunneling selectivity coefficients might vary at the atomic scale. Guillamón *et al.* have reported in Ref. [51] atomic scale modulations of the tunneling spectra in this material which, in our model can be well described by a small modulation of $T_{S,L}$ at the atomic scale. This would be due to the change in $T_{S,L}$ depending on the tip position, respectively, above a Se atom or a hole, as confirmed by our DFT calculations (Secs. IV E and IV F).

B. Tunneling along the a/b axis

In a second step, we have measured the tunneling conductance for a $NbSe_2$ sample with a different orientation. For this purpose, we have fabricated special tips with $NbSe_2$ samples glued on their side on a standard platinum-iridium tip [see schematics in Fig. 2(b)]. A typical conductance spectrum is shown in Fig. 2(b), with a fit using the two-gap proximity effect model as described previously, with the tunneling selectivity fully towards the "small-gap" band (green) and, for comparison, towards the large-gap band (red). The other parameters are unchanged in the fits within the uncertainty mentioned above. For this orientation, it is clear from the fit that the small-gap is dominantly probed, as opposed to the nominal c-axis experiment. This demonstrates that the tunneling selectivity depends clearly upon the sample orientation as in the case of MgB_2.

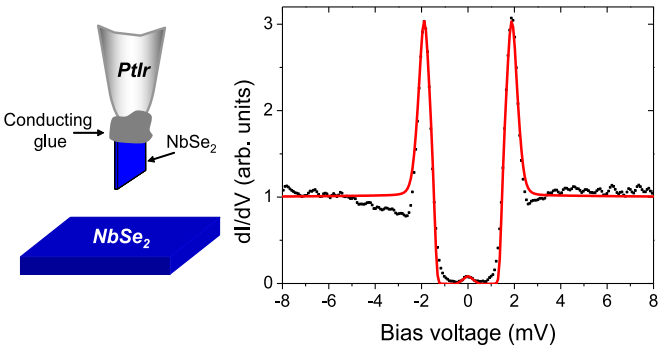

FIG. 4. (Color online) (Left) Scheme of the tunneling junction: the tip is oriented in the a/b axis while the sample is c-axis oriented. (Right) Tunneling conductance of the SIS junction at $T = 2.3$ K. The spectrum is fitted with the McMillan model, assuming a tunneling selectivity towards the small-gap band for the tip ($T_S = 1$, $T_L = 0$) and the large-gap band for the sample ($T_S = 0$, $T_L = 1$). The tip and sample are described by the same parameters as before.

This important point is further checked by using a SIS junction with a $NbSe_2$ tip and a c-axis oriented sample. For a SIS junction, the tunneling current is given by

$$I(V,z) = I_0 \exp(-2\,\alpha_k\, z) \int_E N_{\text{tip}}(E) N_{\text{sample}}(E + eV) \times [f(E) - f(E + eV)]\, dE,$$

where $f(E)$ is the Fermi-Dirac function, $N_{\text{tip}}(E)$ and $N_{\text{sample}}(E)$ are, respectively, the DOS of the tip and the sample. As shown in Fig. 4, the SIS tunneling conductance is well fitted assuming that a full tunneling selectivity towards the small-gap band for the tip (i.e., $T_S = 1$ and $T_L = 0$) and towards the large-gap band for the sample (i.e., $T_S = 0$ and $T_L = 1$), therefore confirming the previous results.

We should note that there are some small deviations of the fit from the experimental curve inside the gap, which could result from a small contribution of a third band (see Sec. V B). In some of the SIS spectra, small dips are also visible outside the gap and could be related to particular surface conditions [52].

C. Temperature dependence of the tunneling conductance

The tunneling spectra for a SIS junction [see Fig. 5(b), $NbSe_2$ tip-$NbSe_2$ sample] as well as for SIN (superconductor-vacuum-normal) junction [see Fig. 5(a), $NbSe_2$ tip-gold sample] were measured as a function of temperature. The conductance curves were fitted at each temperature with the McMillan model for a two-gap superconductor as described in Sec. III A. The same parameters were used for both SIS and SIN junctions.

From the fits, we can deduce the temperature dependence of the intrinsic gaps $\Delta_L^0(T)$ and $\Delta_S^0(T)$. Note that $\Delta_S^0(T)$ is close to zero for all temperatures. In addition, the theoretical dependence of the intrinsic gaps with temperature can be

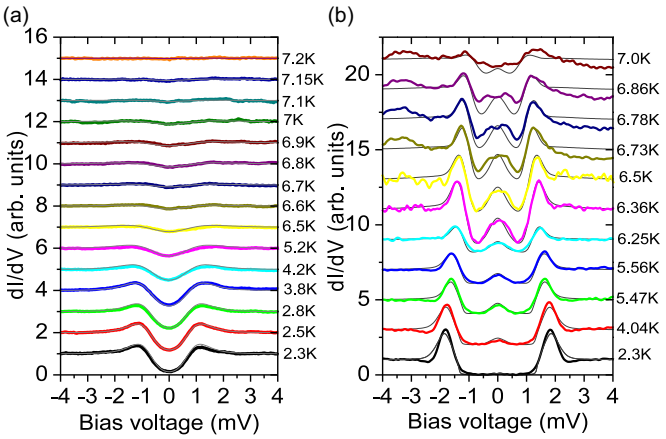

FIG. 5. (Color online) (a) Temperature dependence of the tunneling conductance obtained for a SIN junction with a $NbSe_2$ tip oriented along the a/b axis and a gold sample and corresponding McMillan fit (thin lines). (b) Temperature dependence of the tunneling conductance obtained for a SIS junction with a $NbSe_2$ tip oriented along the a/b axis and a c-axis oriented sample, and corresponding McMillan fit (thin lines). The data are fitted with the McMillan model for a two gap superconductor with the same parameters for the tip and sample: $\Delta_S^0 = 0$ meV, $\Gamma_{SL} = 3$ meV, and $\Gamma_{LS} = \frac{N_S(E_F)}{N_L(E_F)} = \Gamma_{SL}/3$. The intrinsic large-gap Δ_L^0 is the adjustable parameter. In the SIS case, the spectra are fitted with the McMillan model, assuming a tunneling selectivity towards the small-gap band for the tip ($T_S = 1$, $T_L = 0$) and towards the large-gap band for the sample ($T_S = 0$, $T_L = 1$). In the SIN case, we assume a full tunneling towards the small-gap band ($T_S = 1$, $T_L = 0$). At each temperature, the fit gives the value of the intrinsic large-gap $\Delta_L^0(T)$, with $\Delta_S^0(T) = 0$.

obtained from the self-consistent equations:

$$\Delta_i^0 = \lambda_{ii} \int_0^{\hbar\omega_i} dE \tanh\left(\frac{E}{2k_BT}\right) \mathrm{Re}\left[\frac{\Delta_i(E)}{\sqrt{E^2 - \Delta_i^2(E)}}\right] + \lambda_{ij}\sqrt{\frac{N_j}{N_i}} \int_0^{\hbar\omega_{ij}} dE \tanh\left(\frac{E}{2k_BT}\right) \mathrm{Re}\left[\frac{\Delta_i(E)}{\sqrt{E^2 - \Delta_i^2(E)}}\right], \quad (4)$$

where $\lambda_{ii} = V_{ii}N_i$ are the intraband electron-phonon coupling constants of each band, while $\lambda_{ij} = V_{ij}\sqrt{N_iN_j}$ is the interband electron-phonon coupling constant of the Suhl-Matthias-Walker model [15].

While in the most general case, the intrinsic gaps result from both intraband and interband pair coupling, for $NbSe_2$, interband pair coupling can be neglected, but not interband quasiparticle scattering. Fitting Eqs. (3) and (4) to the SIN and SIS spectra (Fig. 5), we find $\lambda_{12} = 0$ and that only the large intrinsic gap is not zero: $\lambda_{22} \approx 0.5$ and $\lambda_{11} = 0$. The corresponding phonon frequency extracted from the fit is $\hbar\omega_2 \approx 6.55$ meV. This shows unambiguously that the small gap is induced by proximity effects as a result of quasiparticle interband coupling, similarly to the case of MgB_2 [31].

The temperature dependence of the intrinsic large-gap, $\Delta_L^0(T)$, deduced from the fits of the tunneling spectra at each temperature is shown in Fig. 6(a) (squares). This dependence is compared to the theoretical expectation $\Delta_L^{0,\mathrm{th}}(T)$, shown as a continuous curve in Fig. 6(a), obtained using Eq. (4) and the low-temperature gap value, together with the critical temperature of $NbSe_2$. A reasonably good agreement is found between the extracted $\Delta_L^0(T)$ and the theoretical dependence $\Delta_L^{0,\mathrm{th}}(T)$. From the calculation, we also deduce the theoretical temperature dependence of the peak to peak gap $\Delta_{S,L}^{\mathrm{pp,th}}(T)$ in the small/large partial DOS $N_{S,L}(E)$ as well as that of the excitation gap $\Delta^{\mathrm{ex,th}}(T)$ [Fig. 6(b)], which can also be compared to the corresponding value deduced from the fit at each temperature. Such plots are often found in the literature of multigap superconductors. Nevertheless, our analysis clearly shows that despite the fact that $NbSe_2$ shows two different SC gaps, only one intrinsic gap is necessary to describe well the tunneling conductance spectra and their evolution as a function of temperature.

D. Two-band model versus distribution of gaps

As already mentioned, the tunneling conductance in $NbSe_2$ was interpreted previously in terms of a continuous gap distribution [9]. In this phenomenological model, the tunneling DOS is described by a weighted sum of BCS DOS: $N(E) = \sum_i g(\Delta_i) N_{\mathrm{BCS}}(E, \Delta_i)$, where $g(\Delta_i)$ is a distribution function describing the probability of having a gap value Δ_i. Following the model of Ref. [9], we have determined the two gap distributions $g(\Delta_i)$ needed to reproduce the DOS of the large and small-gap bands shown in Figs. 6(c) and 6(d), which were calculated by solving the self-consistent equations in the McMillan model. These distributions are shown in Fig. 7.

At low temperature, the distribution function found for the large-gap DOS exhibits two well-defined peaks around 0.77 and 1.16 meV. One notes that their positions are close to the peak-to-peak "gaps" in the McMillan DOS shown in Fig. 6(b). The distribution function found for the small-gap is strikingly different from that of the large-gap. In particular, it exhibits a single peak at 0.76 meV. More importantly, one notices that in some energy ranges, the distribution function has negative values. This demonstrates that it is not possible to properly reproduce the DOS of the small-gap band with a gap distribution having only positive weights. This is due to the very peculiar shape of the peaks of the small-gap DOS [Fig. 6(c)], whose amplitude decreases more rapidly than $\sim 1/\sqrt{E - \Delta}$ close to the gap edge. The same conclusion would of course have been obtained by directly fitting the conductance curve obtained in the tunneling experiment with the tip oriented in the a/b axis. Thus, while the DOS of the large-gap band can be fitted by a gap distribution, this is not the case for the DOS of the small-gap band.

At higher temperature, the large-gap distribution function evolves towards a distribution with a single peak. In addition, for both the small and large gaps, the distribution becomes more and more peaked as the temperature increases and gets very close to BCS, with the same gap value for both bands near the critical temperature. This behavior is in fact very different from that expected in the Suhl, Matthias, and Walker model, which in Ref. [9] is believed to explain the temperature evolution of the two gap distributions. Indeed, in this model, the ratio between the two gaps should first increase when the temperature increases. This behavior is at variance with what is observed in Fig. 7, where the energy of the maxima of both

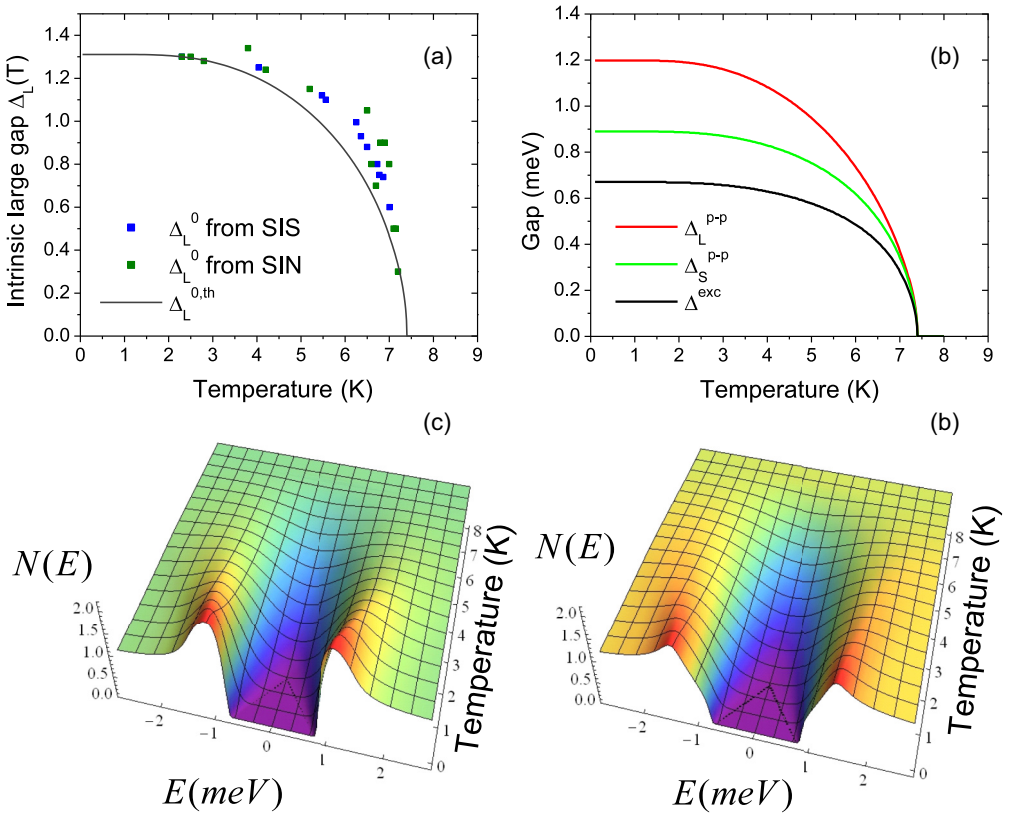

FIG. 6. (Color online) (a) Temperature dependence of the intrinsic large-gap $\Delta_L^0(T)$ deduced from the fits for the SIN ($NbSe_2$ tip-gold sample) (green squares) and SIS junction ($NbSe_2$ tip-$NbSe_2$ sample) (blue squares) compared to the theoretical value $\Delta_L^{0,th}(T)$ calculated by the resolution of the self-consistent equations (4) (black line). (b) Theoretical temperature dependence of the excitation gap $\Delta^{ex,th}$ (for a given temperature, $\Delta^{ex,th}$ is equal to the maximum energy at which $N(E) = 0$, curve in black) and of the peak to peak small and large gaps (in red and green, respectively) $\Delta_{S,L}^{pp,th}$ which are defined as the peak to peak value in the calculated partial DOS for the small and large gap $N_S(E)$ and $N_L(E)$. (c) Temperature dependence of the partial DOS for the small-gap band $N_S(E)$ calculated by the resolution of the self-consistent equation. (d) Temperature dependence of the partial DOS for the large-gap band $N_L(E)$.

distribution functions decrease continuously with increasing temperature. Moreover, the observation of the collapse of the two gaps towards a single BCS like signature close to T_C (see curves in Fig. 7 close to $T = 7$ K) is opposite to the model of Ref. [15], which predicts two very different gaps very close to T_C. On the other hand, such a behavior is a remarkable feature of the quasiparticle mediated interband coupling (as in Schopohl and Scharnberg's model [33]).

To conclude, these series of experiments and analyses leads us to three major conclusions. (i) Tunneling data of $NbSe_2$ can be explained in terms of a two-band proximity effect within the McMillan model. Superconductivity arises in one band, where the electron-phonon coupling constant is large, and is induced in a second band by quasiparticle interband scattering. (ii) The tunneling selectivity has to be taken into account in order to reproduce the different tunneling spectra measured along various crystal orientations. (iii) Tunneling towards the c axis (a/b axis) leads to the observation of a large (small) gap.

However, two points remain to be elucidated: (i) with respect to the band structure, which band corresponds to which gap? (ii) As it is now well established [17], the Se bands contribute an additional branch to the Fermi surface (i.e., the Se based pancake), so its role must be elucidated with respect to the SC properties.

To clarify these aspects, we first discuss the electronic structure of $NbSe_2$ and its implication for the tunneling results on the basis of first-principles DFT calculations. We then consider the possible role of the low-temperature CDW transition occurring in this material below 33 K on the superconductivity.

IV. DFT CALCULATIONS

A. Electronic structure of $NbSe_2$

The electronic structure of $NbSe_2$ has been calculated a number of times in the literature [17,18,22,23,25,53,54]; here we just highlight some aspects which are relevant in order to understand the signatures of multigap superconductivity in the tunneling spectroscopy of $NbSe_2$. The calculated band structure is shown in Fig. 8. The details of the calculations are given in Appendix A. There are three partially filled bands, the two upper ones having niobium 4d as the dominant character (except around Γ), whereas the lower is mostly based on selenium orbitals. From now on these bands will be referred to as band 3, 2, and 1, respectively. This is in contrast with the situation for a single $NbSe_2$ layer where only the two niobium 4d based bands are partially filled.

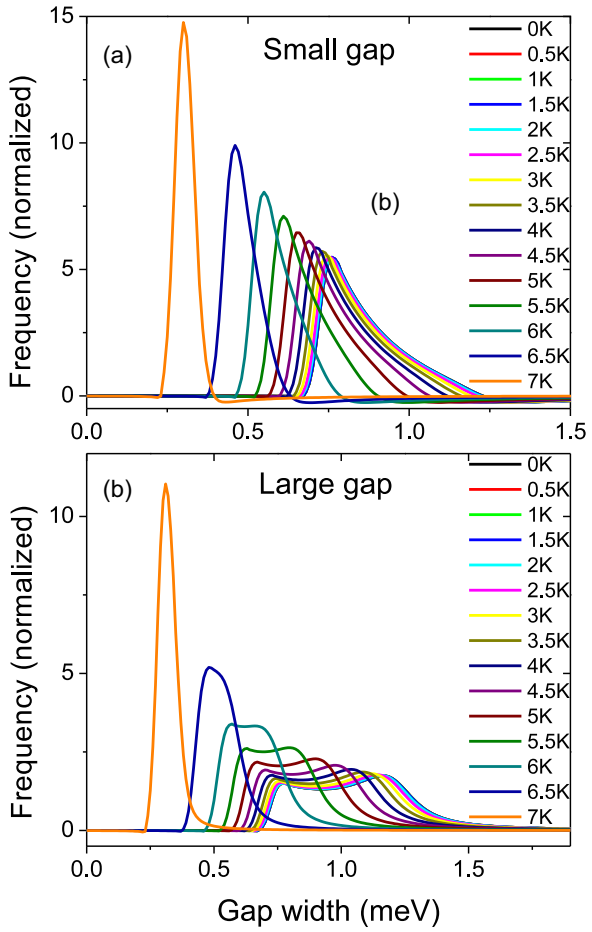

FIG. 7. (Color online) Small (a) and large (b) gaps distributions obtained by fitting the DOS shown in Figs. 6(c) and 6(d), calculated self-consistently as a function of temperature, with a weighted sum of BCS DOS, following the empirical model of Rodrigo *et al.* [9].

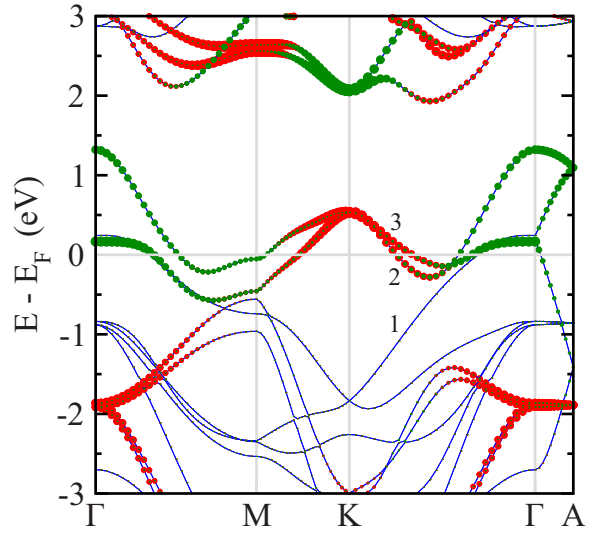

FIG. 8. (Color online) Calculated band structure for $NbSe_2$ where the size of the green and the red circles is proportional to the niobium d_{z^2} and $d_{xy}/d_{x^2-y^2}$ character, respectively. $\Gamma = (0,0,0)$, $M = (1/2,0,0)$, $K = (1/3,1/3,0)$, and $A = (0,0,1/2)$ in units of the reciprocal hexagonal lattice vectors.

The calculated Fermi surface (see Fig. 9) contains three different contributions. First, a pancakelike contribution centered at the Γ point arising from the selenium based band. Second, a pair of warped cylinders centered at Γ arising from the two partially filled niobium 4*d* bands. Third, a pair of warped cylinders centered at K arising also from the two partially filled niobium 4*d* bands. The cylinders occur in pairs because there are two layers per repeat unit and thus there are in-phase and out-of-phase combinations of the single-plane niobium bands. The two cylinders around Γ, as well as those around K, merge at the border of the Brillouin zone because there the phase factors are such that the interlayer interactions vanish. Although both pairs of cylinders around Γ and K originate from the same bands, their character strongly changes from one region to the other : whereas the niobium character is mostly d_{z^2} around Γ it is $d_{xy}/d_{x^2-y^2}$ around K (see Fig. 8).

For simplicity, from now on, we will refer to the cylinders centered at the Γ point (respectively the K point) of the Brillouin zone as the "Nb Γ cylinders" (respectively the "Nb K cylinders") since they mostly arise from the Nb bands.

B. Contribution of the different orbitals to the partially filled bands

In order to correlate the partially filled bands states to the STM images, it is essential to have a clear idea of what is the relative weight of the different orbital contributions, i.e., niobium d_{z^2}, niobium $d_{xy}/d_{x^2-y^2}$ and selenium, for the different parts of the Fermi surface (i.e., in the two different pairs of cylinders and in the pancake around Γ). The pancake is strongly based on the selenium orbitals. Of particular interest are the middle and upper partially filled bands. Their orbital contributions are shown in Fig. 10. An important observation is that the selenium contribution to these formally niobium bands is comparable to the individual niobium contributions. As shown in Fig. 11, almost half of this selenium contribution is p_z, i.e., the selenium orbitals perpendicular to the layers. This means that, although globally the metal character prevails in these two bands, there is a very important hybridization with the selenium orbitals, and particularly with the selenium p_z orbitals. Consequently, these p_z states are expected to dominate the tunneling along the c axis (see the calculation of the tunneling current in Sec. IV D), and the Se atoms will be seen in the tunneling images, at least at large distances from the surface.

C. Partial DOS associated with the different portions of the Fermi surface

We report in Table III the partitioning of the bulk total density of states at the Fermi level into niobium and selenium contributions for each of the three partially filled bands. In addition, for the two niobium based bands (i.e., bands 2 and 3), we also separate the contributions into those associated with the cylinders around Γ and the cylinders around K. Since both bands contribute to the two types of cylinders, we define the contribution to the Nb Γ/K cylinders as the sum of the contributions of bands 2 and 3 around Γ/K. The more salient features of the second and third columns of this table are the following. (i) The total contributions to the DOS at the

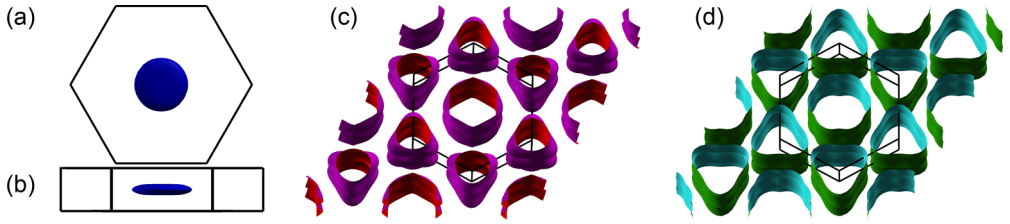

FIG. 9. (Color online) Contribution of band 1 [(a) and (b)], band 2 (c), and band 3 (d) to the Fermi surface for NbSe$_2$.

Fermi level of the upper niobium-based band (i.e., band 3) are considerably larger than those of the lower niobium-based band (i.e., band 2). (ii) For both niobium-based bands, the contribution of the Nb K cylinders is always larger than that of the Nb Γ cylinders. (iii) The contribution of the lower selenium band (i.e., band 1) is small. (iv) The ratio between the contribution of the Nb K cylinders versus Nb Γ cylinders to the total DOS at the Fermi level is 2.7.

The origin of these values is developed in detail in Appendix B. From the inspection of the values of the second and third columns of this table (Nb and Se contributions), one could naively expect that the local DOS probed by STS spectroscopy will be dominated by a large contribution from the Nb K cylinders, a lesser contribution from the Nb Γ cylinders, and finally an even smaller contribution from the selenium based pancake. Surprisingly, this is not what is found in the calculation, as shown in the following.

D. Calculated tunneling STM images

We now consider STM imaging within the Tersoff-Hamman approximation [55], where the current at a given tip position is proportional to the LDOS at that point, integrated over the standard energy window given by the tip-surface potential difference $(E_F, E_F + eV)$.

We stress that the LDOS approximation takes into account the lowest-order tunneling transition matrix approximation for spherically symmetric tip states. In this approximation, tunneling along the axis perpendicular to the surface involves the "tunneling cone" both in real and reciprocal spaces. As a consequence, for tunneling along the c axis of our sample, states with zero and nonzero $k_{//}$ are probed and contribute differently to the tunneling current.

Our images correspond to constant current images, showing the maps of heights that produce a constant tip-surface current. Instead of specifying the value of the current (which is the situation encountered in an experiment), we choose a particular value of the density of states and plot the corresponding constant DOS surface.

In Fig. 12, we show the calculated STM image for a specific DOS isovalue (5×10^{-5} elec/eV/unit cell). The image is made of bright spots centered at the selenium atom positions. When the different contributions of the pancake, the Nb Γ and Nb K cylinders to this image are separated, the three calculated images have practically the same shape, although with different DOS contribution. Thus tunneling in the three portions of the Fermi surface is dominated by the electronic states originated from the selenium atoms, whereas the niobium atoms are not visible in standard tunneling conditions.

As shown in Fig. 12, these calculations are in agreement with experimental results showing the hexagonal atomic selenium lattice (note that for small tip-surface distances, the underlying Nb atoms have been also experimentally seen in the tunneling images [56]). We thus conclude that the Se contribution for each of the three different Fermi surface portions plays a crucial role in the tunneling process.

At this point it is important to note that actual calculations for the $(3a \times 3a \times c)$ CDW modulated structure below 30 K (see the discussion in Appendix C) show that the CDW has only a minor effect on the Se orbitals as well as in the relative weight of the Nb orbitals in the Fermi level region so that the main conclusions of our analysis should still hold after the CDW transition.

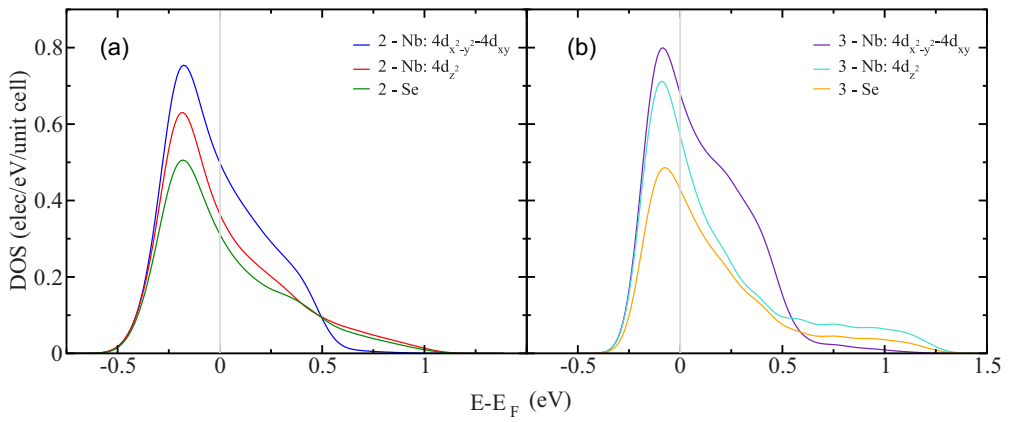

FIG. 10. (Color online) Contributions of the selenium, niobium d_{z^2} and niobium $d_{xy}/d_{x^2-y^2}$ orbitals to the density of states associated with the (a) middle -2- and (b) upper -3- partially filled bands.

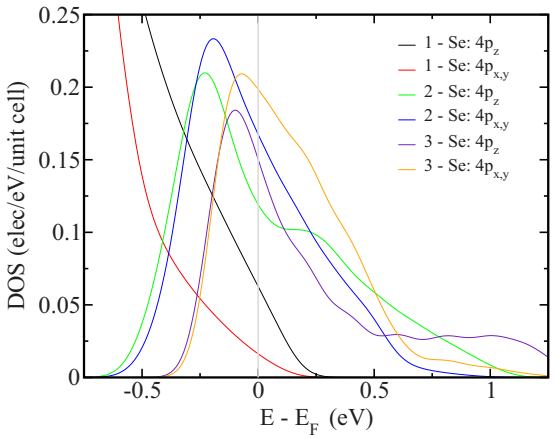

FIG. 11. (Color online) Contributions of the selenium p_z and selenium $p_{x,y}$ orbitals to the density of states associated with the lower (1), middle (2), and upper (3) partially filled bands.

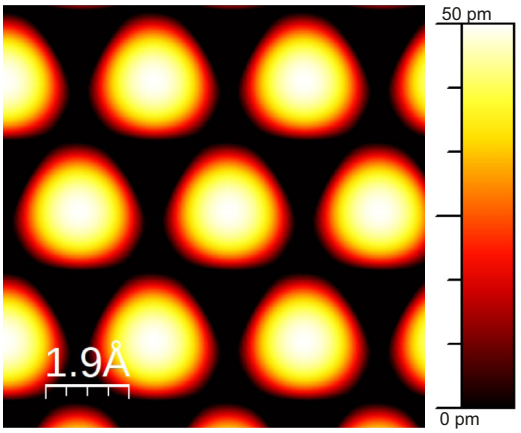

FIG. 12. (Color online) Calculated STM image for $NbSe_2$ (obtained for an iso-DOS value of 5×10^{-5} elec/eV/unit cell).

E. Tunneling selectivity

The key aspect when trying to use the calculated images in understanding the origin of the proposed two-gap superconductivity in this material lies in evaluating the relative weight of the tunneling current due to each of the three components of the Fermi surface. From the Tersoff and Hamman analysis [55], it is expected that the contribution of the states with small wave vector parallel to the surface will decay slower in vacuum and thus give a dominant contribution to the current for large tip-surface distance. It is also stressed that, even if it is not the dominant term, the states near the Brillouin zone boundary may also give a significant contribution.

A precise analysis requires the calculation of the tunneling current as a function of the height of the tip, which reflects how the different contributions in the DOS decrease in vacuum. We have studied the decay of the current $I(z)$ with the tip height z at different positions of the x,y plane for the three different components of the Fermi surface. $I(z)$ is expected to roughly vary exponentially as $I \approx Ae^{-\alpha z}$. If the exponential dependence holds, we can easily obtain α by fitting the calculated $I(z)$.

In some cases, the $I(z)$ curves do not correspond to a single exponential, but rather display two exponential regimes (with two different slopes). This can also be understood within the Tersoff and Hamman model [55]. Far from the surface (where the potential is roughly constant and equal to the vacuum potential), the wave functions can be expressed as

$$\psi_{\mathbf{k}}(x,y,z) = \sum_{G_x}\sum_{G_y} C_{\mathbf{k}}(\mathbf{G}) e^{i(\mathbf{G}+\mathbf{k})\cdot\mathbf{r}} e^{-\alpha_{\mathbf{k}+\mathbf{G}} z}, \tag{5}$$

where $C_{\mathbf{k}}(\mathbf{G})$ is the Fourier component of the wave function at a reference plane (taken as z = 0), $\mathbf{G} = (G_x, G_y)$ the surface reciprocal lattice vectors and $\mathbf{r} = (x,y)$ is the in-plane position. The decay of the corresponding Fourier component with z is thus given by

$$\alpha_{\mathbf{k}+\mathbf{G}} = \sqrt{\kappa^2 + (\mathbf{k}+\mathbf{G})^2}, \tag{6}$$

where κ^{-1} is the standard decay length determined by the work function, ϕ, (i.e., $\kappa = \frac{\sqrt{2m\phi}}{\hbar}$ where m is the electron mass).

From this formula, it is apparent that the wave functions have different Fourier components with different decay lengths into the vacuum. The decay length of a given state depends both on the $\mathbf{G}$ vector of that component, and on the parallel surface momentum $\mathbf{k}$. At large distances from the surface, the $\mathbf{G} = \mathbf{0}$ component will dominate, with a decay $\alpha_{\mathbf{k}} = \sqrt{\kappa^2 + \mathbf{k}^2}$. In this case, the decay of the wave function is determined by both the work function and the wave vector of the states at the Fermi surface, giving a dominant contribution near the Γ point. For distances closer to the surface, several $\mathbf{G}$ will contribute, leading to different decay rates. The results of the fits to $I(z)$ are shown in Table IV. For each component of the Fermi surface, a similar inverse decay length is found ($\sim$1.31 Bohr^{-1}) corresponding to a typical decay length of 0.4 Å. A second exponential is needed for the component

TABLE III. Bulk total and partial DOS for the different bands at the Fermi level around Γ and K (in electrons/eV/unit cell). In the text, Nb Γ/K cylinders refers to the sum of the contributions of bands 2 and 3 around Γ/K.

	DOS (Total)	DOS (Nb contribution)	DOS (Se contribution)	DOS (Se_{p_z} contribution)
Band 1 around Γ	0.117	0.035	0.080	0.062
Band 2 around Γ	0.359	0.239	0.121	0.066
Band 3 around Γ	0.337	0.260	0.080	0.032
Band 2 around K	0.731	0.528	0.203	0.052
Band 3 around K	1.175	0.848	0.331	0.117

TABLE IV. Inverse decay length extracted from exponential fits of I vs z.

Contribution	Position	α-exp 1 (Bohr^{-1})	α-exp 2 (Bohr^{-1})
Pancake	At atom	1.3049 ± 0.0011	–
	At hollow	1.3016 ± 0.0004	–
Cylinder at Γ	At atom	1.3144 ± 0.0016	–
	At hollow	1.3093 ± 0.0007	–
Cylinder at K	At atom	1.3066 ± 0.0006	1.66 ± 0.04
	At hollow	1.3064 ± 0.0006	–

of the cylinders around K, indicating a faster decay of one contribution of the local DOS relatively close to the surface.

F. Contribution of the different portions of the Fermi surface to the tunneling current

The ratio of the local DOS in vacuum associated with the Nb Γ cylinders and Nb K cylinders plotted as a function of the distance from the surface is shown in Fig. 13. For most values of the tip-surface distance in the STM experiment (5–10 Å), the local DOS due to the Nb Γ cylinders is around twice as large as that originating from the Nb K cylinders. In view of the calculated local DOS values for the bulk (see Table III), this is a surprising result since the bulk DOS shows the opposite behavior. However, it can be explained by taking into account the larger relative weight of the Se p_z orbitals around Γ than around K, an effect which is enhanced at the surface, and the signs of the mixing coefficients of the orbitals for a given wave vector (see the discussion in Appendix D).

Let us now turn the attention to the possible role of the Se based pancake of the Fermi surface in understanding the origin of the different superconductivity gaps as probed by the tunneling experiments. Three-quarters of the local density of states at the Fermi level associated with this Se based pancake originate from the Se p_z orbitals so that some degree of interband coupling with the Nb Γ cylinders and/or the Nb K cylinders might be expected. If the contributions to tunneling of the Nb Γ cylinders and the Se based pancake are taken together, it becomes the dominant contribution to the tunneling process when compared with the contribution of the Nb K cylinders (Fig. 13, red curve). Recall that this occurs despite the dominant contribution of the Nb K cylinders over that of the Nb Γ cylinders to the total DOS at the Fermi level for the bulk (see Table III). However, if the contribution to tunneling of the Se based pancake is added to the contribution of the Nb K cylinders, it also becomes the dominant contribution to the tunneling process when compared to the contribution of the Nb Γ cylinders (Fig. 13, green curve).

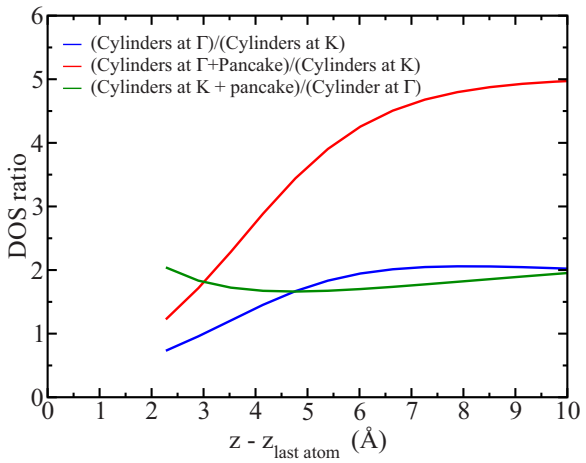

FIG. 13. (Color online) Ratios of the calculated DOS for the various portions of the Fermi surface as a function of the distance from the surface.

Let us note that these results do not depend, at least qualitatively, on the actual type of approach chosen (on top of a Se atom, on top of the hollow, or intermediate) for tip to surface distances relevant for the present measurements. The weight in the tunneling current arising from each FS portion almost does not vary with the tip position, except at short tip-surface distances. Indeed, the contribution of the Nb Γ cylinders with respect to that of the Nb K cylinders is then larger between Se atoms at short distances ($z < 3.5$ Å) than above a Se atom, where z is the tip-surface distance. For larger distances, one recovers qualitatively the results described above (Fig. 13). These very small changes of the tunneling selectivity coefficients at the atomic scale may be responsible for the small modulation of the tunneling spectra, as observed by Guillamón *et al.* [51].

Consequently, our calculations show that, assuming that there is some coupling between the cylinders and the pancake portions of the Fermi surface, the Se based pancake can either reinforce or reverse the noted predominance of the Nb Γ cylinders over the Nb K cylinders in the tunneling. Thus, in order to make the link between the tunneling selectivity and the identification of the two bands associated with the McMillan model, it is crucial to focus on the role of the Se based pancake. This issue is further elaborated in Sec. V.

V. DISCUSSION

A. Linking the small and large gap bands to the Fermi surface sheets

The study of the band structure of $NbSe_2$ by means of DFT calculations gives us the respective contributions of the different Fermi surface sheets to the DOS at the Fermi level (see Table III). Moreover, from the analysis of our experimental tunneling data, we have deduced the ratio of the partial DOS corresponding to the small and the large-gap bands: $N_S(E_F)/N_L(E_F) \sim 1/3$. This information should enable the identification in k space of the Fermi sheets corresponding to the small and large gap bands, or at least to propose a reasonable scenario.

The two Nb Γ cylinders (as well as the two Nb K cylinders) nearly touch and are of the same electronic nature. If one adds together the theoretical DOS contribution of both Nb Γ cylinders (corresponding to the portions around Γ of bands 2 and 3), one obtains 0.7 elect eV^{-1} unit cell^{-1} (i.e., 26% of the total DOS at E_F) while the contribution of the Nb K cylinders (bands 2 and 3 around K) gives 1.9 elect eV^{-1} unit cell^{-1} (i.e., 70% of the total DOS). Thus the ratio between these two partial DOS (that around Γ divided by that around

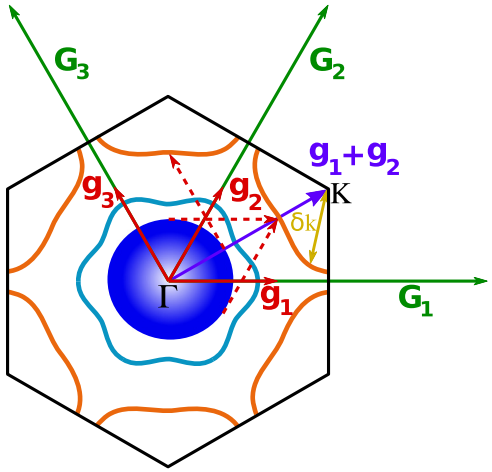

FIG. 14. (Color online) Schematic view of the Fermi surface of $NbSe_2$. The wave vectors of the charge density wave $\vec{g}_i = \frac{1}{3}\vec{G}_i$ (where G_i are the basis vectors of the reciprocal space of $NbSe_2$ above the CDW phase transition temperature) link the selenium pocket around Γ (dark blue area) to the cylinders around K (orange lines) at different points of the first Brillouin zone.

K) is 0.37, a value which is very close to the one inferred from our tunneling data: 0.33 (see Sec. III A). The immediate conclusion is that the small gap DOS is associated with the Nb Γ cylinders and the large-gap DOS with the Nb K cylinders. However, as shown in Fig. 13 (blue line), the contribution of the Nb Γ cylinders to tunneling should dominate over that of the Nb K cylinders. This is not what is observed in the measured tunneling spectra [5,9,36].

To resolve this apparent paradox, there are two important aspects that must be taken into account. First, the existence of the Se pocket around Γ, and second, the charge density wave state present at low temperature. Both have strong implications for the tunneling selectivity and the interband coupling, as we discuss below. The existence of the Se-based pancake (Figs. 9 and 14) has been confirmed experimentally, for instance using ARPES [10,18] or magnetoresistance measurements [17]. As mentioned before, it is strongly based on the Se p_z orbitals. Thus, as established by our calculations (see Fig. 13), the Se-based states should strongly contribute to the tunneling current and a question arises regarding their possible coupling to the Nb bands.

The second aspect to consider is that the low-temperature Fermi surface is more complex than indicated in Fig. 14 due to the CDW state existing below the transition temperature $T_{CDW} \approx 30$ K [3]. In the CDW state the system exhibits a nearly commensurate $(3a \times 3a \times c)$ superstructure [3,21,28]. This may play a significant role in both the interband coupling mechanism as well as in the tunneling selectivity. In fact, taking into account the CDW state leads to a qualitative model in good agreement with the tunneling measurements.

Assuming a commensurate $(3a \times 3a \times c)$ superstructure after the transition, the CDW leads to a reduced hexagonal Brillouin zone with 1/9th of the parent area. It is instructive to consider the extended zone scheme and to look for equivalent k points in the nonreduced (parent) Brillouin zone. In particular, as a result of the new periodicity, the center of the first Brillouin zone, Γ, becomes equivalent to the parent K point since $\Gamma\vec{K} = \vec{g}_1 + \vec{g}_2$, with $\vec{g}_1 = \frac{1}{3}\vec{G}_1$ and $\vec{g}_2 = \frac{1}{3}\vec{G}_2$ (see Fig. 14 where $\vec{G}_i$ are the basis vectors of the parent reciprocal lattice of $NbSe_2$). Consequently, the tunneling probability to electronic states belonging to a pocket around K, will involve new wave functions with an inverse decay length given by $\alpha_k = \sqrt{\delta k^2 + \kappa^2}$ (instead of the former $\alpha_k = \sqrt{(\vec{K} - \delta\vec{K})^2 + \kappa^2}$) where $\vec{\delta k}$ is a vector joining the K point to the nearest FS sheet (see Fig. 14). Clearly, due to the CDW state, tunneling to the Nb K cylinders states gets considerably enhanced.

The CDW state might also play a role in the interband coupling. Indeed, as seen in Fig. 14, the two wave vectors of the charge density wave $\vec{g}_1 = \frac{1}{3}\vec{G}_1$ and $\vec{g}_2 = \frac{1}{3}\vec{G}_2$ precisely link the small selenium pocket around Γ to the portions of the cylinders around K having high DOS. For this reason, we expect a strong coupling mediated by the charge density wave between those two areas of the Fermi surface. As will be shown in the following section, when the coupling is sufficiently strong ($\geqslant$10 meV), the Se Γ pocket and the Nb K cylinders behave as one single band, explaining thereby why the tunneling spectra along the c axis reflect the large-gap band.

The foregoing arguments invoke a usual electron-phonon intraband pairing in one of the two bands (leading to the intrinsic gap Δ_L^0), the large intrinsic gap being associated with the larger DOS. Another hypothetical scenario should also be mentioned. The pairing mechanism could involve an interband pair-pair scattering with a negative coupling constant leading to the reverse situation : the large gap is then associated with the smaller DOS sheet. This hypothesis has been proposed in iron-based superconductors [29] with an interesting sign-reversed order parameter as a consequence. In this case, the large-gap band could be associated with the Nb Γ cylinders coupled to the Se pocket, while the small gap band could in this case be associated with the Nb K cylinders. However, this scenario, requiring an exotic pairing mechanism, seems at present unlikely for $NbSe_2$.

B. A three-band model calculation

The strong coupling effect may be further illustrated by a three-band model calculation. Let us consider three bands (see Fig. 15) with intrinsic gaps $\Delta_1^0 = 0$ meV, $\Delta_3^0 = 0$ meV, and $\Delta_2^0 = 1.4$ meV. The parameters of bands 1 and 2 correspond to the values found for the small-gap (band 1) and large-gap (band 2) bands of $NbSe_2$. Band 1 is thus weakly coupled to band 2 and very weakly coupled to band 3. We then studied the evolution of the partial DOS as a function of the interband coupling parameter Γ_{32} between bands 2 and 3. The ratios of the interband scattering parameters have been chosen such that they correspond to the calculated DFT ratios of the partial DOS: $\frac{N_1(E_F)}{N_2(E_F)} = 1/3$, $\frac{N_3(E_F)}{N_2(E_F)} = 1/16$, and $\frac{N_3(E_F)}{N_1(E_F)} = 1/6$ (we recall that band 1 is associated with the Nb Γ cylinders, band 2 with the Nb K cylinders, and band 3 with the Se pocket around Γ).

The interband coupling between bands 2 and 3 leads to an induced gap in band 3. As seen in Fig. 16, when Γ_{32} increases, the DOS of band 3 gets close to that of band 2. For very large $\Gamma_{32} \geqslant 50$ meV, one recovers a situation very similar to an effective two-band model with a new

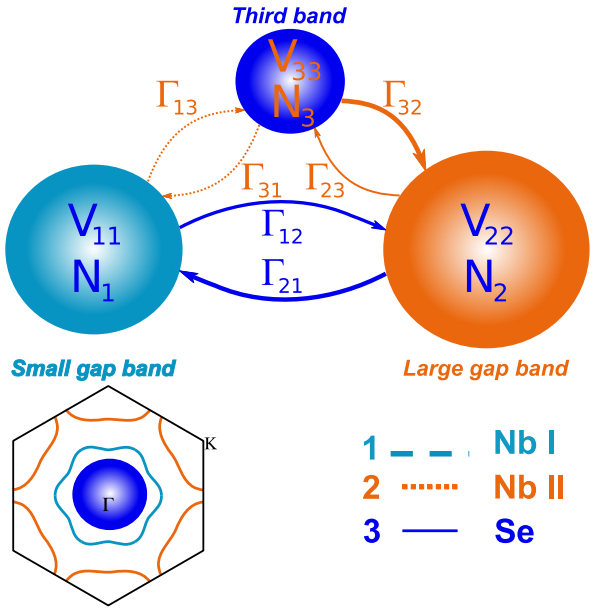

FIG. 15. (Color online) Schematic view of the possible interband couplings between those bands associated with the three different Fermi surface components. Band 1 (2) corresponds to the Nb cylinders around Γ (K), while band 3 corresponds to the Se pocket around Γ.

effective band constituted by bands 2 and 3. Thus, for a large coupling strength, the model shows that bands 2 and 3 are indistinguishable from one single band. In Fig. 17, we plot the corresponding tunneling conductance assuming a complete tunneling selectivity towards band 3 (i.e., with tunneling weights $T_1 = 0$, $T_2 = 0$, and $T_3 = 1$). For a large coupling $\Gamma_{32} \geqslant 50$ meV, the tunneling conductance is very close to the one predicted in the two-band model, with a complete selectivity towards the band with the large-gap, corresponding well to the experimental observation.

In summary, we propose that the CDW state has strong implications for both the interband coupling between the Se-based pancake and the K cylinders as well as for the probability to tunnel towards electronic states around the K point, due to the first Brillouin zone reconstruction. As a result, this gives rise to a strong contribution to the tunneling conductance of the states around K, an essential ingredient for the observation of the large-gap in c-axis tunneling spectra. The analysis above suggests that the band where the large-gap develops is constituted of both the K cylinders and the Se pancake, strongly coupled together through quasiparticle scattering. Moreover, the quasiparticule coupling described in the McMillan model between the Γ and the K cylinders, is likely to be associated to the reduced lattice reciprocal vectors $\vec{g}_1$ and $\vec{g}_2$ of the CDW state.

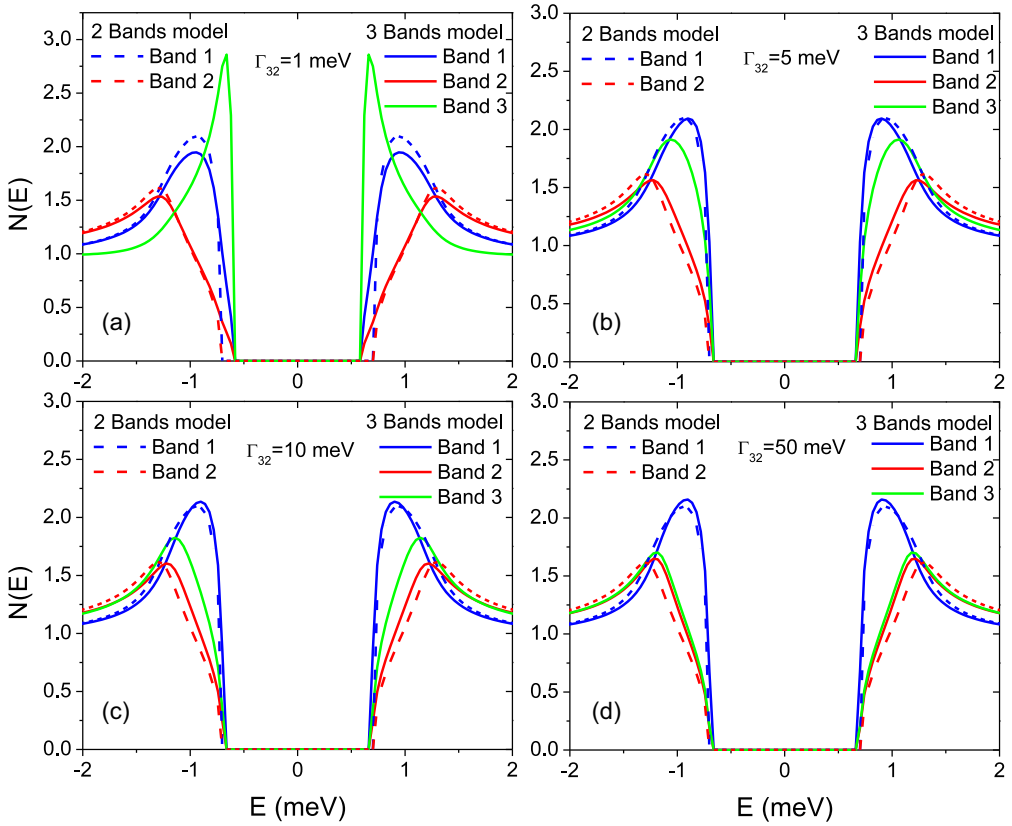

FIG. 16. (Color online) Partial DOS calculated for a three-bands model for different values of the interband coupling parameter between band 2 and band 3: (a) $\Gamma_{32} = 1$ meV, (b) $\Gamma_{32} = 5$ meV, (c) $\Gamma_{32} = 10$ meV, and (d) $\Gamma_{32} = 50$ meV. The intrinsic gaps are $\Delta_1^0 = 0$ meV, $\Delta_2^0 = 1.4$ meV, and $\Delta_3^0 = 0$ meV. The ratio of the partial DOS at the Fermi energy are related to the ratio of quasiparticle scattering between the corresponding bands $\frac{N_1(E_F)}{N_2(E_F)} = \frac{\Gamma_{21}}{\Gamma_{12}} = 1/3$, $\frac{N_3(E_F)}{N_2(E_F)} = \frac{\Gamma_{23}}{\Gamma_{32}} = 1/16$, and $\frac{N_3(E_F)}{N_1(E_F)} = \frac{\Gamma_{13}}{\Gamma_{31}} = 1/6$. The quasiparticle scattering parameters are $\Gamma_{12} = 3$ meV and $\Gamma_{21} = 1$ meV.

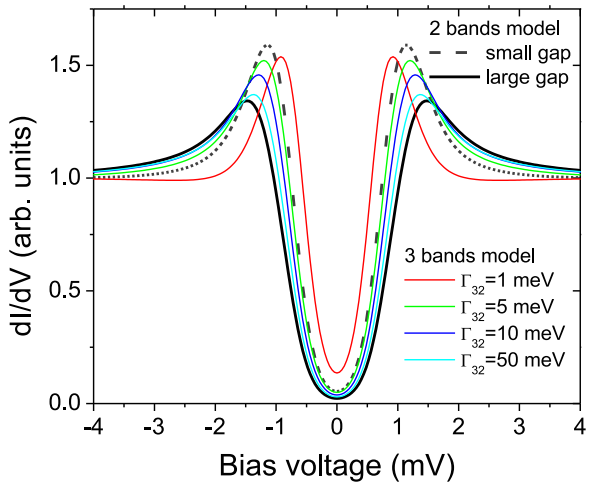

FIG. 17. (Color online) Tunneling conductance dI/dV calculated in the three-band model for different values of the interband coupling parameter between bands 2 and 3: $\Gamma_{32} = 1$, 5, 10, and 50 meV. Dashed line: tunneling conductance expected for the small and large-gap in the two band model.

C. Comparison with $2H$-NbS_2

It is also interesting to compare the tunneling conductance spectra measured on $NbSe_2$ to that reported by Guillamón *et al.* for $2H$-NbS_2 [57]. This material is close to $NbSe_2$, with a superconducting transition temperature of $T_C = 5.7$ K but does not exhibit any charge density wave instability [58]. Fitting their data with our two-band model (Fig. 18), we obtain parameters close to those of $NbSe_2$. The intrinsic gaps are $\Delta_S^0 = 0 \pm 0.05$ meV, $\Delta_L^0 = 1.15 \pm 0.05$ meV, $\Gamma_{SL} = 1.5$ meV, and a ratio $\frac{\Gamma_{LS}}{\Gamma_{SL}} = 1/3 \pm 0.3$. The selectivity weights corresponding to the tunneling towards the two different effective bands are $T_S = 0.4$ and $T_L = 0.6$.

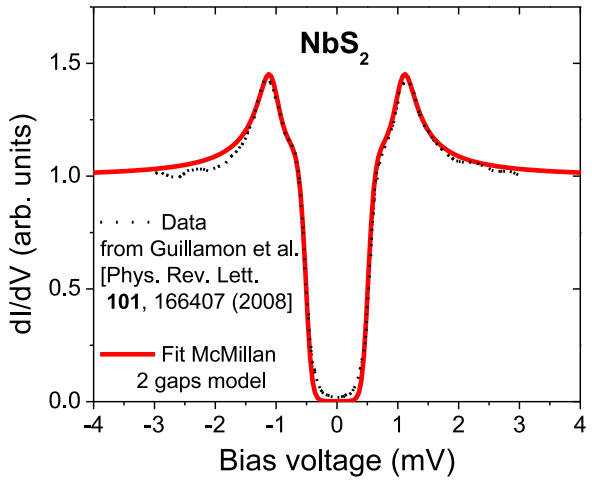

FIG. 18. (Color online) Tunneling conductance dI/dV spectrum from Guillamón *et al.* [57] and fit obtained with our two-band McMillan equations. The parameters for the fit are the following. The intrinsic gaps are $\Delta_S^0 = 0 \pm 0.05$ meV, $\Delta_L^0 = 1.15 \pm 0.05$ meV, $\Gamma_{SL} = 1.5$ meV, and $\frac{\Gamma_{LS}}{\Gamma_{SL}} = 1/3 \pm 0.3$. The selectivity weights corresponding to the tunneling towards the two different effective bands are $T_S = 0.4$ and $T_L = 0.6$. We have used an effective temperature for the fit ($T_{\text{eff}}^{\text{fit}} = 0.5$ K), which includes inelastic processes not taken into account in our model.

We thus find that, as for $NbSe_2$, our approach enables to reproduce the experimental spectra with a very good agreement. This implies that superconductivity develops in one band (or more precisely in one Fermi surface sheet), whereas it is induced in the other band by means of interband coupling mediated by quasiparticle scattering from one band to the other. The ratio found for the coupling parameters Γ_{ij} is very close to the value found for $NbSe_2$. This is in agreement with the similar density of states expected at the Fermi level for the K and Γ cylinders in both material. On the other hand, it is clear from the fits that the tunneling selectivity differs from $NbSe_2$ ($T_S = 0$; $T_L = 1$). This means that in $2H$-NbS_2 there is a more important contribution of the band with the small-gap DOS to the tunneling current than in $NbSe_2$.

In principle, this feature could be explained in two different ways. First, although there is no CDW transition in $2H$-NbS_2 [58], our calculations show that the Fermi surface is very similar to that of $NbSe_2$. In particular, the S-based pancake around Γ is also present. This result is quite robust since calculations for reasonable changes in the cell constants lead only to small changes in the FS shape. As for $NbSe_2$, a similar mechanism for the coupling to the K cylinders could take place through dynamical coupling [26], although a static CDW modulation does not occur in this material. As a result the S based pocket could be strongly coupled to the K cylinders.

The change in the tunneling selectivity coefficients of the two bands (T_S and T_L), would originate from the absence of a real band structure reconstruction due to the absence of the CDW in this material. In addition, the scenario pointed out here to explain the observed differences between the experimental tunneling spectra of $NbSe_2$ and $2H$-NbS_2, is in agreement with the observation that vortices in the first material where the CDW is present have a star shape, while they are circular in the other material, where the CDW is absent [57].

However, another scenario could be considered. While the S pocket exists in the bulk, it could be argued that the S pocket has no states at the Fermi level at the surface layer, as a result of surface relaxation or contamination. Indeed, for $NbSe_2$, we do observe a change in the tunneling selectivity depending on the cleavage conditions. This might be also the case in NbS_2. In this case, the c-axis tunneling originates primarily from both the Nb cylinders around Γ and K, as shown in Sec. IV E. The simplest origin one could think for the suppression of the S based pancake, would be the occurrence of S vacancies, which will raise the Fermi level. Using the bulk calculations we estimate that a large number of vacancies (i.e., 15%) are needed. Thus this mechanism does not seem likely, but it cannot be completely ruled out.

VI. CONCLUSION

We have measured the dI/dV tunneling conductance spectra of $NbSe_2$ by scanning tunneling spectroscopy for two different crystal orientations. Indeed, the tunneling conductance is properly reproduced by the McMillan two-band model. In this framework, superconductivity develops in one

band (with gap value $\Delta_L^0 = 1.4$ meV) and is induced in the second band by a proximity effect in reciprocal space ($\Delta_S^0 = 0$ meV) through interband coupling provided by the scattering of quasiparticles. The data show evidence of a strong tunneling selectivity, which also depends on the crystal orientation: a DOS with a large gap is mainly probed along the c axis while a small-gap DOS is measured along the a/b axis.

To interpret these results, and to link the two gaps to respective bands, a realistic band structure of $NbSe_2$ was calculated using first-principles DFT. The Fermi surface contains three components: a pancakelike Se based contribution around Γ, and two pairs of Nb-based cylinders parallel to c around Γ and K, respectively. The calculated values of the partial DOS at the Fermi energy associated with each of these three components show that the large-gap should be associated with the cylinders around K, while the small gap should correspond to the Γ cylinders. It is quite possible that the gaps on each Fermi surface sheet are anisotropic, a point we did not focus on here. High-resolution ARPES will be helpful to determine the precise k-space variations and ultimately quantify the amount of anisotropy and gap assignment. The analysis of STS quasiparticle interference would also bring some insight into this question.

Finally, our simulations of the tunneling current in the Tersoff-Hamman approximation show that the local DOS probed by STS is dominated by the p_z character of the Se orbitals. Considering that the large-gap DOS should originate from the K cylinders, these results imply that a strong quasiparticle coupling should exist between the Se-based pancake and the K-cylinder Fermi surfaces. Such an interband coupling could be adequately provided by the CDW wave vectors existing in the superconducting phase of $NbSe_2$. The latter mechanism also explains the tunneling spectra measured on the related compound $2H$-NbS_2 although in this case there is not a real CDW transition. This work thus brings a new light on the possible interaction between superconducting and CDW states in $NbSe_2$.

ACKNOWLEDGMENTS

Work in Bellaterra was supported by Spanish MINECO (Grant Nos. CSD2007-00041 and CSD2007-00050, and Nos. FIS2012-37549-C05-05 and FIS2012-37549-C05-02 with joint financing by FEDER Funds from the European Union), and Generalitat de Catalunya (2014SGR301). J.A.S.-G. and P.O. acknowledge support of the Spanish MINECO through the Severo Ochoa Centers of Excellence Program under Grant SEV-2013-0295. J.A.S.-G. was supported by an FPI Fellowship from MINECO. The authors thankfully acknowledge the computer resources, technical expertise and assistance provided by the Red Española de Supercomputación.

APPENDIX A: COMPUTATIONAL DETAILS

DFT calculations were carried out using a numerical atomic orbitals density functional theory (DFT) approach [59,60], which was developed for efficient calculations in large systems and implemented in the SIESTA code [61,62]. We have used the generalized gradient approximation (GGA) to DFT and, in particular, the functional of Perdew, Burke, and Ernzerhof [63]. Only the valence electrons are considered in the calculation, with the core being replaced by norm-conserving scalar relativistic pseudopotentials [64] factorized in the Kleinman-Bylander form [65]. The nonlinear core-valence exchange-correlation scheme [66] was used for all elements. We have used a split-valence double-ζ basis set including polarization functions, optimized for the bulk structure of $NbSe_2$ [67]. The energy cutoff of the real space integration mesh was 300 Ry. The Brillouin zone was sampled using a grid of $(30 \times 30 \times 30)$ k points within the Monkhorst-Pack scheme [68]. The experimental crystal structure was used in the bulk calculations for $2H$-$NbSe_2$ [19] and $2H$-NbS_2 [70]. A symmetrical slab ten and a half unit cells thick based on the experimental bulk structure was used for the calculation of the STM images. In that case, we also used an extra diffuse orbital in the basis set so as to take into account the slab nature of the system [69] and the Brillouin zone was sampled using a mesh of $(30 \times 30 \times 1)$ k points. The geometry of the $(3a \times 3a \times c)$ superstructure was optimized.

APPENDIX B: QUALITATIVE UNDERSTANDING OF THE DENSITY OF STATES

The features of the density of states at the Fermi level can be understood on the basis of the analysis of the wave functions. The two partially filled niobium-based bands, though more heavily based on the metal atoms, contain substantial niobium-selenium antibonding character. The dispersion of these bands results from a subtle equilibrium between direct in plane niobium-niobium interactions (ultimately responsible for the 30 K structural distortion) [22] and niobium-selenium antibonding interactions.

Increasing the niobium d_{z^2} participation in the wave function is accompanied by an increase of the participation of the selenium p_z orbitals. Roughly speaking, increasing the weight of d_{z^2} in the wave function makes the Fermi surface more isotropic within the layer plane and shifts electron density from antibonding levels to the interlayer direction so that the mixing of niobium d_{z^2} orbitals will be less favorable for the subband associated with the interlayer antibonding interactions. Increasing the niobium d_{z^2} participation (and thus the selenium p_z orbitals) increases the interlayer dispersion and reduces the density of states. Thus, keeping in mind the results of Fig. 8, it is easy to understand that the density of states at the Fermi level for both bands is larger for the cylinder around K and that the effect is larger for the upper, interlayer antibonding band.

APPENDIX C: EFFECT OF THE CDW ON THE BAND STRUCTURE

Since our analysis is based on the room-temperature crystal structure whereas the tunneling images are obtained at temperatures below the 30 K transition, we must consider if the structural distortion may noticeably affect the results. The experimental structure of the low-temperature phase was not experimentally known when our study was initiated so that we carried out a structural optimization using a $(3a \times 3a \times c)$ supercell with fixed cell parameters. We obtained two different structures exhibiting a niobium clustering pattern closely

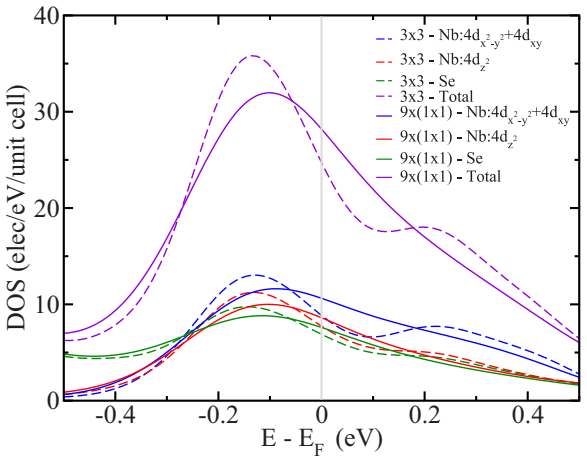

FIG. 19. (Color online) Comparison of the niobium d_{z^2}, niobium $d_{xy}/d_{x^2-y^2}$ and selenium contributions for the normal [noted as $9 \times (1 \times 1)$] and CDW [noted (3×3)] states.

related to those proposed by Brouwer and Jellinek [28] and Moncton, Axe, and DiSalvo [27], respectively. The latter was found to be slightly more stable with a stabilization energy of 7.5 K per formula unit with respect to the non modulated structure.

The projected densities of states for niobium d_{z^2}, niobium $d_{xy}/d_{x^2-y^2}$ and selenium corresponding to the distorted (noted 3×3) and undistorted (noted 1×1) fully optimized structures (with the only restriction of keeping the interlayer c parameter fixed to the experimental value because of the usual problems of DFT with van der Waals interactions) are compared in Fig. 19. There is a small decrease of the DOS at the Fermi level but definitely there is no gap opening. This is in keeping with early resistivity and heat-capacity measurements [71,72] suggesting that the decrease in the density of states at the Fermi level should be of the order of only 1%. It is also in agreement with an independent theoretical study by Calandra *et al* [25]. The lack of a gap opening at the Fermi level is in agreement with a very recent atomic-scale scanning tunneling microscopy study [73], which together with another recent work on the temperature dependence of phonon dispersion [26] provide clear experimental evidence to exclude a Fermi surface nesting mechanism for the 30 K transition. In what concerns the Se contribution to the DOS, the difference is very small so that the modulation should only weakly affect the tunneling.

The main effect of the CDW is a slight rehybridization of the niobium d orbitals. As shown in Fig. 19, there is a small but definite decrease of both the niobium d_{z^2} and niobium $d_{xy}/d_{x^2-y^2}$ orbital contributions when the CDW occurs. However, the decrease of the niobium d_{z^2} contribution is around twice as large as that of the niobium $d_{xy}/d_{x^2-y^2}$ contribution, which means that the CDW brings about a small but non-negligible niobium d orbitals rehybridization. We found similar although smaller variations for $2H$-NbS_2.

APPENDIX D: DISCUSSION ON THE CONTRIBUTION OF THE Γ AND *K* CYLINDERS TO THE TUNNELING CURRENT

For most values of the tip-to-surface distance, the contribution of the cylinders around Γ to the tunneling intensity is around twice as large as that of the cylinders around K (Fig. 13). This may seem a bit surprising if we recall that the respective contributions to the density of states at the Fermi level in the bulk were found to be just the opposite (see Table III).

One can think about two possible origins for this reversal. First, the faster decaying of the contribution of the cylinders around K is due to the **k** selectivity of the tunneling current [55]. It follows from Eq. (6) that the contribution to the tunneling of Fermi surface states with wave vectors near the Brillouin zone center ($\mathbf{k} = 0$) should be larger. Consequently, the contribution of the cylinders around Γ should become larger because of this effect and maybe could overcome the initial difference in DOS at the Fermi level. However, in the present case, we evaluate the effect of this **k** selectivity as leading at most to an increase of about 10% of the calculated value. Consequently, this is not be the main factor behind the dominance of the contribution of the cylinders around Γ.

The main difference between the LDOS arising from the Nb K and Nb Γ cylinders is the nature of the niobium orbitals implicated: d_{z^2} around Γ but $d_{xy}/d_{x^2-y^2}$ around K. This induces a different hybridization of the Se orbitals in the wave function. In the case of the Se atoms at the surface, our detailed calculations show that for the states around Γ, their contribution is more strongly dominated by the p_z orbitals than it is for the states around K. Since the decay of the Se p_z orbitals is in fact slower than that of the Se (p_x, p_y) orbitals, this would lead to a larger decay of the K states at short distances ($z \lesssim 5$ Å) from the surface, while the Γ states having a slower decay will dominate for larger distances ($z \gtrsim 5$ Å). Asymptotically, only the p_z orbitals contribute leading to the equivalence of the decay rates for the Γ and K states, as shown in Table IV.

[1] E. Revolinsky, E. P. Lautenschlager, and C. H. Armitage, Solid State Comm. **1**, 59 (1963).
[2] E. Revolinsky, G. A. Spiering, and D. J. Beernsten, J. Phys. Chem. Solids **26**, 1029 (1965).
[3] J. A. Wilson, F. J. Di Salvo, and S. Mahajan, Phys. Rev. Lett. **32**, 882 (1974).
[4] R. C. Morris and R. V. Coleman, Phys. Lett. A **43**, 11 (1972).
[5] H. F. Hess, R. B. Robinson, and J. V. Waszczak, Phys. Rev. Lett. **64**, 2711 (1990).
[6] L. F. Mattheiss, Phys. Rev. Lett. **30**, 784 (1973).
[7] N. F. Doran, B. Ricco, M. Schreiber, D. Titterington, and G. Wexler, J. Phys. C **11**, 699 (1978)
[8] N. J. Doran, J. Phys. C **11**, 959 (1978).
[9] J. G. Rodrigo and S. Vieira, Physica C **404**, 306 (2004).

[10] T. Yokoya, T. Kiss, A. Chainani, S. Shin, M. Nohara, and H. Takagi, Science **294**, 2518 (2001).

[11] E. Boaknin, M. A. Tanatar, J. Paglione, D. Hawthorn, F. Ronning, R. W. Hill, M. Sutherland, L. Taillefer, J. Sonier, S. M. Hayden, and J. W. Brill, Phys. Rev. Lett. **90**, 117003 (2003); E. Boaknin, M. A. Tanatar, J. Paglione, D. G. Hawthorn, R. W. Hill, F. Ronning, M. Sutherland, L. Taillefer, J. Sonier, S. M. Hayden, and J. W. Brill, Physica C **408–410**, 727 (2004).

[12] C. L. Huang, J.-Y. Lin, Y. T. Chang, C. P. Sun, H. Y. Shen, C. C. Chou, H. Berger, T. K. Lee, and H. D. Yang, Phys. Rev. B **76**, 212504 (2007).

[13] Yan Jing, Shan Lei, Wang Yue, Xiao Zhi-Li, and Wen Hai-Hu, Chin. Phys. B **17**, 2229 (2008).

[14] J. D. Fletcher, A. Carrington, P. Diener, P. Rodière, J. P. Brison, R. Prozorov, T. Olheiser, and R. W. Giannetta, Phys. Rev. Lett. **98**, 057003 (2007).

[15] H. Suhl, B. T. Matthias, and L. R. Walker, Phys. Rev. Lett. **3**, 552 (1959).

[16] J. Bardeen, L. Cooper, and J. Schrieffer, Phys. Rev. **108**, 1175 (1957).

[17] R. Corcoran, P. Meeson, Y. Onuki, P.-A. Probst, M. Springford, K. Takita, H. Harima, G. Y. Guo, and B. L. Gyorffy, J. Phys.: Condens. Matter **6**, 4479 (1994).

[18] K. Rossnagel, O. Seifarth, L. Kipp, and M. Skibowski, D. Voß, P. Krüger, A. Mazur, and J. Pollmann, Phys. Rev B. **64**, 235119 (2001).

[19] A. Meerschaut and C. Deudon, Mat. Res. Bull. **36**, 1721 (2001).

[20] M. Marezio, P. D. Dernier, A. Menth, and G. W. Hull Jr., J. Solid State Chem. **4**, 425 (1972).

[21] J. A. Wilson, F. J. DiSalvo, and S. Mahajan, Adv. Phys. **24**, 117 (1976).

[22] M.-H. Whangbo and E. Canadell, J. Am. Chem. Soc. **114**, 9587 (1992).

[23] M. D. Johannes, I. I. Mazin, and C. A. Howells, Phys. Rev. B **73**, 205102 (2006).

[24] T. M. Rice and G. K. Scott, Phys. Rev. Lett. **35**, 120 (1975).

[25] M. Calandra, I. I. Mazin, and F. Mauri, Phys. Rev. B **80**, 241108 (2009).

[26] F. Weber, S. Rosenkranz, J.-P. Castellan, R. Osborn, R. Hott, R. Heid, K.-P. Bohnen, T. Egami, A. H. Said, and D. Reznik, Phys. Rev. Lett. **107**, 107403 (2011).

[27] D. E. Moncton, J. D. Axe, and F. J. DiSalvo, Phys. Rev. B **16**, 801 (1977).

[28] R. Brouwer and F. Jellinek, Physica B **99**, 51 (1980).

[29] I. I. Mazin, D. J. Singh, M. D. Johannes, and M. H. Du, Phys. Rev. Lett. **101**, 057003 (2008).

[30] C. D. Malliakas and M. G. Kanatzidis, J. Am. Chem. Soc. **135**, 1719 (2013).

[31] H. Schmidt, J. F. Zasadzinski, K. E. Gray, and D. G. Hinks, Physica C **385**, 221 (2003).

[32] W. L. McMillan, Phys. Rev. **175**, 537 (1968).

[33] N. Schopohl and K. Scharnberg, Solid State Commun. **22**, 371 (1977).

[34] M. Nohara, M. Isshiki, F. Sakai, and H. Takagi, J. Phys. Soc. Jpn. **68**, 1078 (1999).

[35] T. Hanaguri, A. Koizumi, K. Takaki, M. Nohara, H. Takagi, and K. Kitazawa, Physica B **329–333**, 1355 (2003).

[36] Y. Noat, T. Cren, F. Debontridder, D. Roditchev, W. Sacks, P. Toulemonde, and A. San Miguel, Phys. Rev. B **82**, 014531 (2010).

[37] D. Sanchez, A. Junod, J. Muller, H. Berger, and F. Lévy, Physica B **204**, 167 (1995).

[38] T. Kiss, T. Yokoya, A. Chainani, S. Shin, M. Nohara, and H. Takagi, Physica B **312–313**, 666 (2002).

[39] T. Valla, A. V. Fedorov, P. D. Johnson, P-A. Glans, C. McGuinness, K. E. Smith, E. Y. Andrei, and H. Berger, Phys. Rev. Lett. **92**, 086401 (2004).

[40] T. Kiss, T. Yokoya, A. Chainani, S. Shin, T. Hanaguri, M. Nohara, and H. Takagi, Nat. Phys. **3**, 720 (2007).

[41] S. V. Borisenko, A. A. Kordyuk, V. B. Zabolotnyy, D. S. Inosov, D. Evtushinsky, B. Büchner, A. N. Yaresko, A. Varykhalov, R. Follath, W. Eberhard, L. Patthey, and H. Berger, Phys. Rev. Lett. **102**, 166402 (2009).

[42] D. J. Rahn, S. Hellmann, M. Kalläne, C. Sohrt, T. K. Kim, L. Kipp, and K. Rossnagel, Phys. Rev. B **85**, 224532 (2012).

[43] J. Kortus, O. V. Dolgov, R. K. Kremer, and A. A. Golubov, Phys. Rev. Lett. **94**, 027002 (2005).

[44] P. Szabó, P. Samuely, J. Kačmarčík, T. Klein, J. Marcus, D. Fruchart, S. Miraglia, C. Marcenat, and A. G. M. Jansen, Phys. Rev. Lett. **87**, 137005 (2001).

[45] F. Giubileo, D. Roditchev, W. Sacks, R. Lamy, D. X. Thanh, J. Klein, S. Miraglia, D. Fruchart, J. Marcus, and P. Monod, Phys. Rev. Lett. **87**, 177008 (2001).

[46] G. Karapetrov, M. Iavarone, A. E. Koshelev, W. K. Kwok, G. W. Crabtree, D. G. Hinks, and S. I. Lee, Physica C **388–389**, 141 (2003).

[47] M. Iavarone, G. Karapetrov, A. E. Koshelev, W. K. Kwok, G. W. Crabtree, D. G. Hinks, W. N. Kang, E.-M. Choi, H. J. Kim, H.-J. Kim, and S. I. Lee, Phys. Rev. Lett. **89**, 187002 (2002).

[48] H. Schmidt, J. F. Zasadzinski, K. E. Gray, and D. G. Hinks, Phys. Rev. Lett. **88**, 127002 (2002).

[49] H. J. Choi, D. Roundy, H. Sun, M. L. Cohen, and S. G. Louie, Nature (London) **418**, 758 (2002).

[50] The parameters used for the fit are in good agreement but are slightly different from those deduced at $T = 2K$. This might come from different surface conditions. One also notes that the fit deviates from the data inside the gap for bias voltages close to the excitation gap. This could further be explained in terms of a three-band model, which would take into account the effect of the Se pocket, as explained in Sec. V B.

[51] I. Guillamón, H. Suderow, F. Guinea, and S. Vieira, Phys. Rev. B **77**, 134505 (2008).

[52] A small dip outside the gap is also present in some of the SIS spectra. This feature could be attributed to a small contribution of the small-gap band due to some surface conditions. As a matter of fact, it has been shown by Noat *et al.* in Ref. [36] that such dips can arise in the SIS spectra of a two-band superconductor when tunneling takes place toward the small-gap band. One needs that one of the two electrode is either a conventional superconductor or the same two-gap superconductor with a tunneling towards the small-gap band.

[53] G. Wexler and A. M. Wolley, J. Phys. C **9**, 1185 (1976).

[54] T. Straub, T. Finteis, R. Claessen, P. Steiner, S. Hüfner, P. Blaha, C. S. Oglesby, and E. Bucher, Phys. Rev. Lett. **82**, 4504 (1999).

[55] J. Tersoff and D. R. Hamann, Phys. Rev. B **31**, 805 (1985).

[56] P. Mallet, W. Sacks, D. Roditchev, D. Défourneau, and J. Klein, J. Vac. Sci. Technol. B **14**, 1070 (1996).

[57] I. Guillamón, H. Suderow, S. Vieira, L. Cario, P. Diener, and P. Rodière, Phys. Rev. Lett. **101**, 166407 (2008).

[58] Y. Hamaue and R. Aoki, J. Phys. Soc. Jpn. **55**, 1327 (1986).
[59] P. Hohenberg and W. Kohn, Phys. Rev. **136**, B864 (1964).
[60] W. Kohn and L. J. Sham, Phys. Rev. **140**, A1133 (1965).
[61] J. M. Soler, E. Artacho, J. Gale, A. García, J. Junquera, P. Ordejón, and D. Sánchez-Portal, J. Phys.: Condens. Matter **14**, 2745 (2002).
[62] E. Artacho, E. Anglada, O. Diéguez, J. D. Gale, A. García, J. Junquera, R. M. Martin, P. Ordejón, J. M. Pruneda, D. Sánchez-Portal, and J. M. Soler, J. Phys.: Condens. Matter **20**, 064208 (2008).
[63] J. P. Perdew, K. Burke, and M. Ernzerhof, Phys. Rev. Lett. **77**, 3865 (1996).
[64] N. Troullier and J. L. Martins, Phys. Rev. B **43**, 1993 (1991).
[65] L. Kleinman and D. M. Bylander, Phys. Rev. Lett. **48**, 1425 (1982).
[66] S. G. Louie, S. Froyen, and M. L. Cohen, Phys. Rev. B **26**, 1738 (1982).
[67] E. Artacho, D. Sánchez-Portal, P. Ordejón, A. García, and J. M. Soler, Phys. Stat. Sol. (b) **215**, 809 (1999).
[68] H. J. Monkhorst and J. D. Pack, Phys. Rev. B **13**, 5188 (1976).
[69] S. García-Gil, A. García, N. Lorente, and P. Ordejón, Phys. Rev. B **79**, 075441 (2009).
[70] F. Jellinek, G. Brauer, and H. Mueller, Nature (London) **185**, 376 (1960).
[71] J. R. Long, S. P. Bowen, and N. E. Lewis, Solid State Commun. **22**, 363 (1977).
[72] J. M. E. Harper, T. H. Geballe, and F. J. DiSalvo, Phys. Lett. A **54**, 27 (1975).
[73] C. J. Arguello, S. P. Chockalingam, E. P. Rosenthal, L. Zhao, C. Gutiérrez, J. H. Kang, W. C. Chung, R. M. Fernandes, S. Jia, A. J. Millis, R. J. Cava, and A. N. Pasupathy, Phys. Rev. B **89**, 235115 (2014).